# MÖSSBAUER SCATTERING STUDIES WITH THE ISOTOPES

## $Os^{186}$, $Os^{188}$, $Eu^{153}$, and $Pr^{141}$

Rollin John Morrison

Department of  Physics

University of Illinois

Ph. D. Dissertation

October 1964

# MÖSSBAUER SCATTERING STUDIES WITH THE ISOTOPES $Os^{186}$, $Os^{188}$, $Eu^{153}$ and $Pr^{141}$

Rollin John Morrison, Ph.D.
Department of Physics
University of Illinois, 1965

The thesis describes the observation of sizable Mössbauer effects with gamma rays of energies up to 155 keV. In order to observe significant effects for transitions with large recoil energies, and therefore small recoilless fractions, the experiments were performed with a scattering geometry.

Some theoretical aspects of Mössbauer scattering are discussed. Calculations of the recoilless and nonrecoilless scattered intensities for single line Lorentzian distributions are presented. The scattered intensities are expressed in terms of a scattering function which contains the parameters of the scatterer. The scattering function has been evaluated for a wide range of values of the recoilless fraction, electronic absorption, thickness, and line width of the scatterer.

The attractiveness and general applicability of the scattering method are demonstrated by the experimental results. The effects observed for the various sources and scatterers are given in the table below. These measurements were made with source and scatterer temperatures below $35^{\circ}$ K.

| Isotope | E , keV | Source | Scatterer | Effect |
|---------|---------|--------|-----------|--------|
| $Eu^{153}$ | 103 | $Sm_2O_3$ | $Eu_2O_3$ | 30% |
| " | " | $SmF_3$ | " | 18% |
| $Os^{186}$ | 137 | Re metal | Os metal | 9.7% |
| $Pr^{141}$ | 145 | $CeO_2$ | $Pr_6O_{11}$ | 4% |
| " | " | $CeF_3$ | " | 3% |
| $Os^{188}$ | 155 | Re metal | Os metal | 6.5% |

The products of the source and scatterer recoilless fractions have been determined from the scattered intensities with the aid of the calculated scattering function. With the assumption that the source and scatterer Debye temperatures $\Theta_D$ were equal, values $\Theta_D = (312 \pm 7)^{\circ}$ K and $\Theta_D = (322 \pm 7)^{\circ}$ K were determined from the scattered intensities for the $Os^{186}$ and $Os^{188}$ measurements. Experiments were performed with higher source and scatterer temperatures. From these measurements we found that the effective Debye temperature increases with temperature and with the magnitude of the recoil energy. Recoilless fractions and Debye temperatures were calculated for all of the measurements. Ferrimagnetic europium iron garnet was also used as a scatterer for the 103 keV transition of $Eu^{153}$. From the magnetic hyperfine pattern observed, the ratio of the excited state and ground state g factors was determined. Using a previously measured value for the ground state magnetic moment we found the value $\mu^{*} = (1.9 \pm 0.2)$ n m for the magnetic moment of the excited state.

## ACKNOWLEDGEMENTS

TABLE OF CONTENTS

# 1. INTRODUCTION

In the six years since its discovery the Mössbauer effect* has become established as a useful tool for the study of problems in chemistry, nuclear physics, and solid state physics. To a large extent its usefulness stems from the fact that low lying nuclear levels of stable isotopes can be found which have lifetimes between $10^{-6}$ and $10^{-10}$ seconds. The corresponding natural widths of the resonance lines are between $10^{-10}$ and $10^{-6}$ eV respectively. With this energy resolution the Mössbauer effect can be used to measure the magnetic dipole, and electric monopole and quadrupole interactions of the nucleus with the fields at the center of the atom. These fields are strongly dependent upon the properties of the crystal lattice and upon the chemical binding.

There are a large number of low-lying nuclear levels of stable isotopes with lifetimes between $10^{-6}$ and $10^{-10}$ seconds. Relatively few, however, lend themselves to easy Mössbauer experiments because the energy $E_\gamma$ of most of the levels is high enough so that the probability for a recoilless emission or absorption is small. In the Debye model the recoilless fraction for a lattice with a temperature of $0°$ K is

$$f = e^{-\frac{3}{2}\frac{E_R}{K\theta}}$$

(1-1)

where the free nucleus recoil energy $E_R$ is given by

---

*For a discussion of the Mössbauer effect see Frauenfelder[1] and Boyle and Hall.[2]

$$E_R = \frac{E_\gamma^2}{2Mc^2} .$$

(1-2)

Here $Mc^2$ is the rest energy of the nucleus, k is the Boltzmann constant and $\theta_D$ is the Debye temperature of the lattice. The criterion for a sizable recoilless fraction is that $E_R$ be less than or comparable with the typical lattice energy $k\theta_D$. With the normal transmission arrangement, experiments with recoilless fractions less than about three percent are difficult and have limited usefulness. For example, with rare earth oxides which have Deybe temperatures $\sim 200°$ K this would mean that 100 keV is about the upper limit for useful transitions. Other materials have higher Debye temperatures but few experiments have been performed with energies over 100 keV. The highest energy Mössbauer effect that has been observed with a transmission experiment is the 134 keV transition of $Re^{187*}$.[3]

This thesis describes the observation of sizable Mössbauer effects with gamma rays of energies up to 155 keV by means of resonant scattering. The advantage of scattering over the normal transmission method can be seen from Figs. 1 and 2. In the case of transmission both recoillessly and nonrecoillessly emitted gamma rays of the energy $E_\gamma$ pass through the resonant absorber and are counted. If the relative energy shift of the source with respect to the absorber (which includes the relative Doppler shift, $S = \frac{v\,E_\gamma}{c}$ ) is less than or of the order of the line width of the nuclear level, resonant absorption of the recoillessly emitted gamma rays occurs in the absorber and a lower count rate results. A typical curve of the transmission versus the absorber velocity is shown. In the limit that

---

[*]The highest energy Mossbauer effect that has been previously reported is the 137 keV transition of $Os^{186}$ (Ref. 4 and 5) which was observed with a scattering geometry.

# TRANSMISSION  GEOMETRY

ABSORBER

COUNTER

SOURCE

VELOCITY $v$

DOPPLER SHIFT $S = \dfrac{v}{c} E_\gamma$
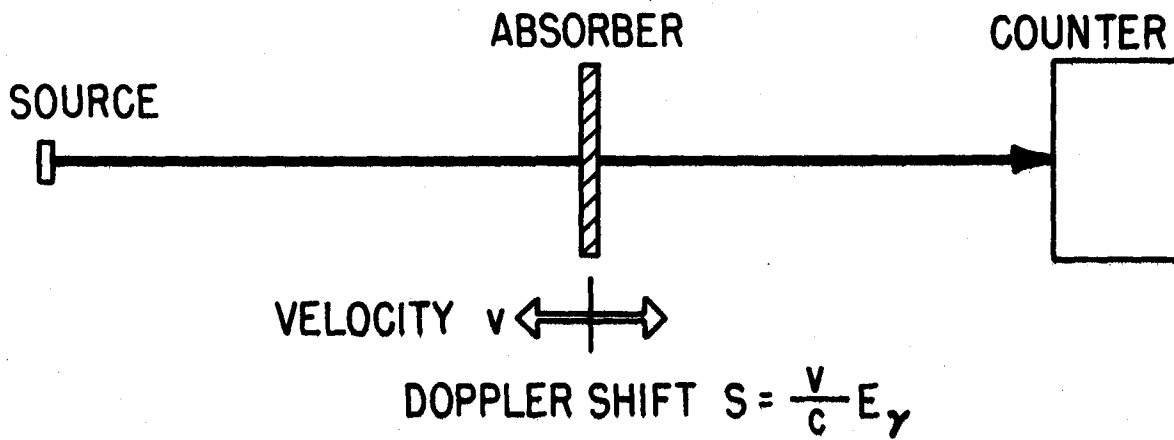
# COUNT  RATE  vs.  ABSORBER  VELOCITY

counts/sec

D

$T(\infty)$

$T(0)$

$v$ (cm/sec)
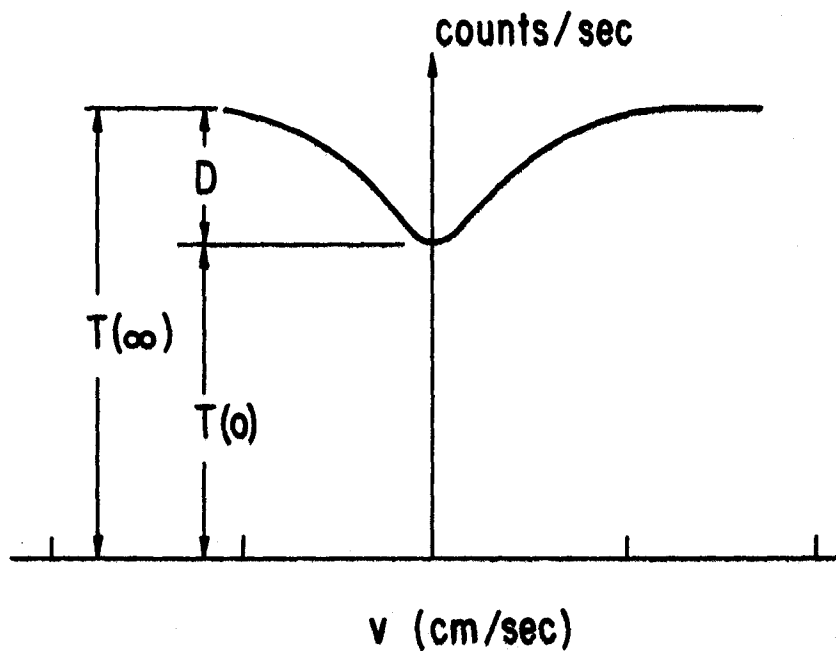
Fig. 1.  The arrangement for a Mössbauer transmission experiment
and a typical curve of the transmission vs. absorber
velocity.

# SCATTERING GEOMETRY



**SOURCE**

v ⟵ + − ⟶

**MOVING RESONANT SCATTERER**

**SHIELDING**

**SCATTERED GAMMA RAY**

**COUNTER**
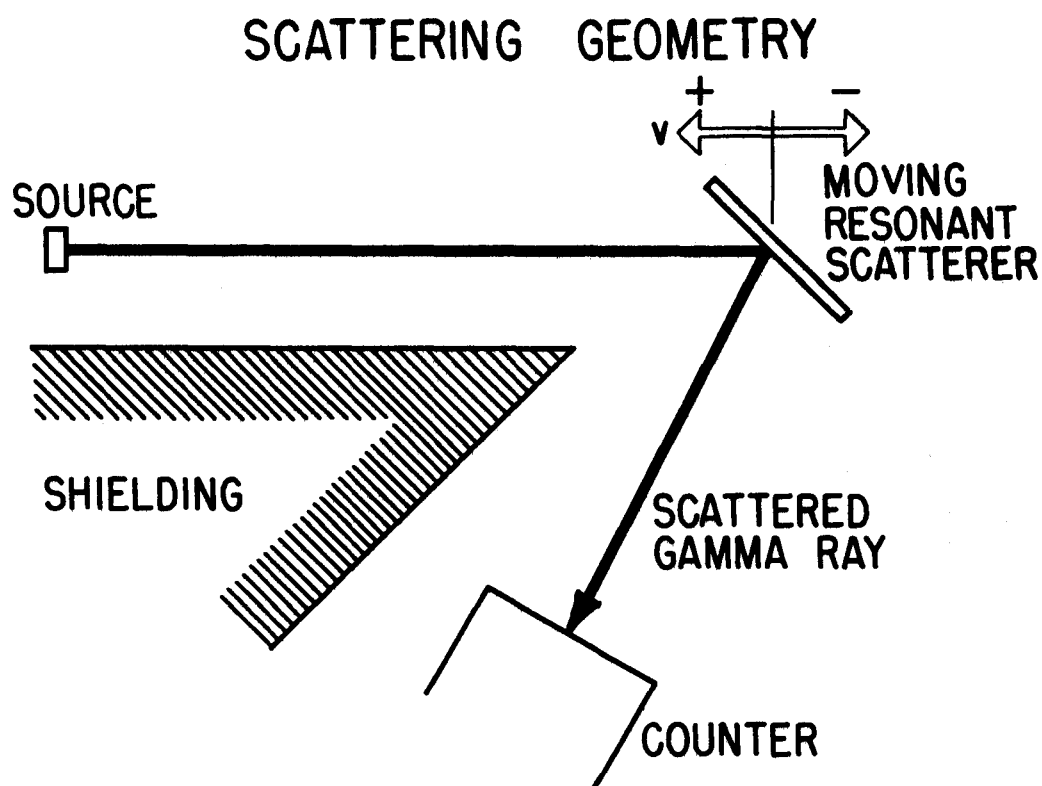
# COUNT RATE vs. SCATTERING VELOCITY

counts/sec

$N_T(0)$

B

v (cm/sec)
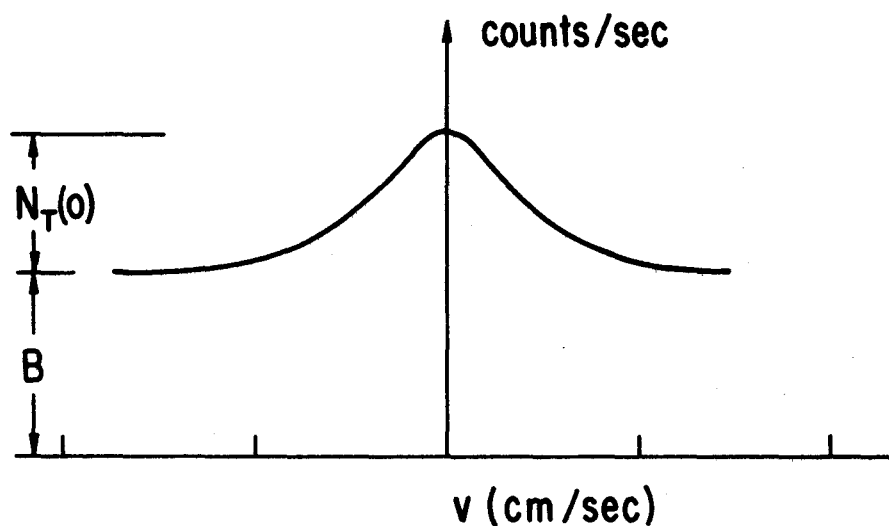
**Fig. 2.** The arrangement for a Mössbauer scattering experiment and a typical curve of the scattered count rate vs. the scatterer velocity.

the absorber is very thick the magnitude of the effect, D/T(inf), approaches the value of the recoilless fraction. With a transmission arrangement the size of the effect is limited because the nonrecoilless gamma rays are counted.

The scattering geometry does not have this intrinsic limitation. A typical arrangement is shown in Fig. 2. The counter is shielded from the source so that in the ideal case only recoillessly emitted gamma rays which are resonantly scattered will be counted. The resonant scattering process can be visualized as a resonant absorption followed by a re-emission.[*] The re-emitted radiation can be either recoillessly or nonrecoillessly emitted gamma rays, or conversion electrons. In the ideal case there are counts only when the source and scatterer are on resonance. A typical curve of the scattered count rate as a function of the scatterer velocity is shown. The count rate off resonance, B, is the background caused by Compton scattering and other processes. The size of the effect is $N_T(0)/B$ where $N_T(0)$, the resonantly scattered intensity, depends upon the source and scatterer recoilless fractions. If the background count rate is low, large effects can be observed even with small recoilless fractions.

The first two chapters of this thesis are devoted to a discussion of the scattering method. Theoretical aspects of resonant scattering are discussed and calculations of the resonantly scattered intensities are presented.[**] The calculations are used to determine the recoilless fractions of the source and scatterer from the scattered intensity. The experimental method is described.

---

[*] The details are discussed in Sec. 2.1.

[**] These calculations have been submitted for publication.[6]

The attractiveness and general applicability of the scattering method is demonstrated by the results presented in the last two chapters. Experiments were performed with the 103, 137, 145, and 155 keV gamma rays of $Eu^{153}$, $Os^{186}$, $Pr^{141}$, and $Os^{188}$ respectively.* The sizable resonant peaks observed made it possible to measure the recoilless fractions, isomer shifts, and in the case of $Eu^{153}$ the magnetic moment of the excited state.

---

*The Mössbauer effect in $Eu^{153}$ was first observed by De Nercy, Langevin and Spighel.[7,8] The $Os^{186}$ transition was investigated by Barrett and Grodzins.[4,5] Our preliminary results with $Os^{186}$ and $Os^{188}$ have been published.[9]

## 2. RESONANT SCATTERING

### 2.1 Cross Sections

In the early history of the Mössbauer effect there were differences of opinion concerning the dependence of the Mössbauer resonant scattering cross section on the recoilless fraction f'. Both experimental work[10,11,12] and theoretical arguments[13,14,15] support the fact that if the lifetime of the nuclear state is long compared with the crystal vibration times $\sim 10^{-13}$ sec, the recoilless (elastic) part of the resonant cross section is proportional to $f'^2$ while the total resonant cross section* is proportional to f'.

The differential scattering cross section for the resonant scattering of a gamma ray by a nucleus embedded in a crystal with a lattice transition from the initial state i to the final stage f is

$$\frac{d\sigma_{fi}}{d\Omega} = \frac{\sigma_o'}{4\pi} \frac{\Gamma'^2}{4} \frac{W(\theta)}{1+\alpha} w_{fi} \, ,$$
(2-1)

where $\Gamma'$ is the width of the excited nuclear level, $\alpha$ is the internal conversion coefficient, $\theta$ is the scattering angle, and $W(\theta)$[5] is the angular correlation function corresponding to a gamma-gamma cascade with a spin sequence $I_{gr} \xrightarrow{abs} I_{exc} \xrightarrow{em} I_{gr}$, where $I_{gr}$ and $I_{exc}$ are the spins of the nuclear ground and excited states respectively. The nuclear absorption cross section $\sigma_o'$ is given by[16]

$$\sigma_o' = \frac{2\pi}{|\vec{k}_{inc}|^2} \frac{2I_{exc}+1}{2I_{gr}+1} \frac{1}{1+\alpha} \, ,$$
(2-2)

---

*In the total resonant cross section we include only processes in which the scattered radiation is a gamma ray.

where $\vec{k}_{inc}$ is the wave vector of the incident gamma ray.

The factor $w_{fi}$ depends upon the properties of the lattice and is given by[17)]

$$w_{fi} = \left| \sum_j \frac{\langle f | e^{-i\vec{k}_{scat} \cdot \vec{r}} | j \rangle \langle j | e^{i\vec{k}_{inc} \cdot \vec{r}} | i \rangle}{E_{inc} - E_0 - (\epsilon_j - \epsilon_i) + i\Gamma/2} \right|^2 \tag{2-3}$$

In this expression $\vec{k}_{scat}$ is the wave vector of the scattered gamma ray, $\vec{r}$ is the position of the scattering nucleus, $\epsilon_i$ and $\epsilon_j$ are the crystal energies for the eigenstates i and j, $E_0$ is the energy of the scatterer resonance, and $E_{inc}$ is the energy of the incident gamma ray. For the lifetimes usually encountered with the Mössbauer effect the width $\Gamma'$ is between $10^{-10}$ and $10^{-6}$ eV. This width is much smaller than the typical energy level spacing of the lattice $\epsilon_j - \epsilon_i \sim 10^{-2}$ eV. If the incident gamma ray energy is near the scatterer resonance, $E_{inc} - E_0 \sim \Gamma'$, then only the state j = i contributes to the sum. We can then write Eq. (2-3)

$$w_{fi} = \frac{1}{(E_{inc} - E_0)^2 + \Gamma'^2/4} \left| \langle f | e^{-i\vec{k}_{scat} \cdot \vec{r}} | i \rangle \right|^2 \left| \langle i | e^{i\vec{k}_{inc} \cdot \vec{r}} | i \rangle \right|^2 \tag{2-4}$$

No energy is given to the lattice if the lattice remains in the initial state. The probability for a recoilless scattering is proportional to

$$w_{ii}^R = \frac{1}{(E_{inc} - E_0)^2 + \Gamma'^2/4} \left| \langle i | e^{-i\vec{k}_{scat} \cdot \vec{r}} | i \rangle \right|^2 \left| \langle i | e^{i\vec{k}_{inc} \cdot \vec{r}} | i \rangle \right|^2 \tag{2-5}$$

For a given temperature we have a probability distribution of initial states i. If we perform a thermal average over the initial states we obtain

$$w^R = \{w_{ii}^R\}_T = \frac{1}{(E_{inc} - E_0)^2 + \Gamma'^2/4} f'^2 \tag{2-6}$$

Here $\{\ \}_T$ indicates a thermal average and the recoilless fraction f' is defined

$$f' = \left\{ \left| \langle i | e^{-i\vec{k}\cdot\vec{r}} | i \rangle \right|^2 \right\}_T . \tag{2-7}$$

The differential cross section for the resonant scattering of a gamma ray with no recoil energy loss is then given by

$$\frac{d\sigma_R}{d\Omega} = \frac{f'^2 \sigma_0'}{4\pi} \ \frac{1}{1+\alpha} \ \frac{W(\theta)}{\left[ 2/\Gamma' \ (E_{inc} - E_0) \right]^2 + 1} \tag{2-8}$$

For the total resonant scattering probability in which energy may or may not be given to the lattice one obtains

$$w_i^t = \frac{1}{(E_{inc} - E_0)^2 + \Gamma'^2/4} \sum_f \left| \langle f | e^{-i\vec{k}_{scat}\cdot\vec{r}} | i \rangle \right|^2 \left| \langle i | e^{i\vec{k}_{inc}\cdot\vec{r}} | i \rangle \right|^2 \tag{2-9}$$

We can write

$$\sum_f \left| \langle f | e^{-i\vec{k}_{scat}\cdot\vec{r}} | i \rangle \right|^2 = \sum_f \langle i | e^{i\vec{k}_{scat}\cdot\vec{r}} | f \rangle \langle f | e^{-i\vec{k}_{scat}\cdot\vec{r}} | i \rangle \tag{2-10}$$

and using completeness,

$$\sum_f | f \rangle \langle f | = 1, \tag{2-11}$$

we have

$$w_i^t = \frac{1}{(E_{inc} - E_0)^2 + \Gamma'^2/4} \left| \langle i | e^{i\vec{k}_{inc}\cdot\vec{r}} | i \rangle \right|^2 . \tag{2-12}$$

If we perform a thermal average over the initial states we obtain

$$\overline{w^{+}} = \frac{1}{(E_{inc} - E_0)^2 + \Gamma'^2/4} \, f'_{)}$$  (2-13)

and the differential cross section for the total resonant scattering is

$$\frac{d\sigma_T}{d\Omega} = \frac{f'\sigma_0'}{4\pi} \frac{1}{1 + \alpha} \frac{W(\theta)}{[2/\Gamma'(E_{inc} - E_0)]^2 + 1} .$$  (2-14)

From this discussion we see that for the nuclear lifetimes usually encountered with the Mössbauer effect the resonant scattering process can be visualized as a resonant absorption with a probability proportional to $f'$, and a subsequent re-emission with the probability $\frac{f'}{1 + \alpha}$ that the re-emitted radiation is a recoillessly emmitted gamma ray.

## 2.2 Scattering from Resonant Nuclei in a Solid State Environment

If recoilless gamma rays from a Mössbauer source are incident upon a resonant scatterer the resonantly scattered intensity depends upon the line shape and relative energy shift of the source, and the thickness, isotopic abundance, electronic absorption, recoilless fraction, and line shape of the scatterer. We have calculated the recoilless and nonrecoilless parts of the scattered intensity for single line Lorentzian source and scatterer line shapes and for various values of the scatterer parameters. These calculations, which are presented in Sec. 2.3, are subject to the assumptions which are discussed in the remainder of this section.

### 2.21 Interference with Rayleigh Scattering.[18] For gamma ray energies of the order 14 keV and lower there is significant interference between

Rayleigh scattering by the atom and nuclear resonant scattering. The
scattered intensity versus velocity curve exhibits an asymmetric shape
since the cross section contains a term proportional to the shift of the
gamma ray energy from the scatterer resonance. For energies of 100 keV or
higher this effect is negligible for all but forward scattering because
the Rayleigh cross section is small. More than three fourths of the
Rayleigh scattering takes place with scattering angles $\theta < \theta_0^*$ where

$$\theta_0 = 2 \sin^{-1}\left(2.6 \times 10^{-2} Z^{1/3} \frac{mc^2}{E}\right). \tag{2-15}$$

For $\theta > \theta_0$ the differential Rayleigh cross section per unit solid angle is

$$\frac{d\sigma_{Ray}}{d\Omega} = \frac{8.67 \; 10^{-33}}{\sin^3 \frac{1}{2}\theta}\left(Z \frac{mc^2}{E}\right)^3 \frac{1 + \cos^2\theta}{2} \; cm^2, \tag{2-16}$$

where Z is the nuclear charge of the scattering atom, E is the energy of
the incident gamma ray, and $mc^2$ is the electron rest energy. For the 103
keV gamma ray of $Eu^{153}$, for example, we have $\theta_0 \sim 60°$, and at $\theta = 180°$

$$\frac{d\sigma_{Ray}}{d\Omega} \sim 2.5 \; 10^{-25} \; cm^2.$$

This is small compared with the product of the isotopic abundance, a, and
the nuclear resonant cross section,

$$a \frac{d\sigma_{nuc}}{d\Omega} \sim 6 \; 10^{-23} \; cm^2.$$

---

$^*$These expressions are essentially those of Franz.[19] They have been
discussed and checked experimentally by Moon.[20]

2.22 _Diffraction Peaks at Bragg Angles._ Since part of the resonant scattering is coherent, diffraction peaks occur at Bragg angles due to the regular lattice structure. This effect is discussed by O'Connor and Black[18] for single crystals. With our geometry the Bragg effects should cause a negligible error in the calculation of the scattered intensities since we used a powder scatterer and since our scatterer and counter solid angles were quite large.

2.23 _Lorentzian Line Shape._ A third assumption made in the calculations is that the energy distribution of the incident gamma rays and the scatterer cross section have Lorentzian line shapes. Although these line shapes are generally distorted as a result of solid state effects, it is approximately valid in many cases to assume a broadened Lorentzian[21,22] shape where the cross section on resonance $\sigma_0$ is given

$$\sigma_0 = \sigma_0' \frac{\Gamma_{nat}}{\Gamma'} .$$

(2-17)

In this expression $\Gamma_{nat}$ is the natural width of the excited state and $\Gamma'$ is the effective width of the scatterer.

## 2.3 Scattered Intensities

From Sec. 2.1 we see that the total differential scattering cross section contains two parts, a recoilless part Eq. (2-8), and a nonrecoilless part which is given by the difference between the total resonant scattering Eq. (2-14) and the recoilless part Eq. (2-8),

$$\frac{d\sigma_{NR}}{d\Omega} = \frac{d\sigma_T}{d\Omega} - \frac{d\sigma_R}{d\Omega} = \frac{f'(1-f')}{4\pi} \frac{\sigma_0'}{1+\alpha} \frac{W(\theta)}{\left[2/\Gamma'(E_{inc} - E_0)\right]^2 + 1} .$$

(2-18)

The two parts of the scattered radiation have intensities which are different functions of the scatterer thickness since the recoilless part is subject to both resonant and electronic reabsorption while the nonrecoilless part is absorbed only by electronic processes.

Eqs. (2-8) and 2-18) are valid only if the resonance line shape is not distorted. It is convenient to write the cross sections in terms of a resonant absorption coefficient $\mu(E)$ which has the dimension length$^{-1}$, and which reduces to

$$\mu(E) = \frac{n\, \sigma_0\, f'}{[2/\Gamma'\, E]^2 + 1} \tag{2-19}$$

if the line is Lorentzian. Here E is the energy measured from $E_0$, the resonance energy of the scatterer, and n is the number of Mössbauer nuclei per $cm^2$. Then we can write the scattering cross sections in units length$^{-1}$ per fractional solid angle for recoilless and nonrecoilless scattering, respectively,

$$n\, \frac{d\sigma_R}{d\Omega/4\pi} = \frac{f'\, W(\theta)}{1+\alpha}\, \mu(E), \tag{2-20}$$

and

$$n\, \frac{d\sigma_{NR}}{d\Omega/4\pi} = \frac{(1-f')\, W(\theta)}{1+\alpha}\, \mu(E), \tag{2-21}$$

Consider the resonant scattering of a distribution $I_R(E,\, S_1)$ of recoilless gamma rays from a Mössbauer source by a foil of thickness t with scattering cross sections given by Eqs. (2-20) and (2-21) and an electronic absorption coefficient $\mu_e$. Here $S_1$ is the energy difference between the energy of the source and the resonance of the scatterer. The distribution $I_R(E,\, S_1)$ is normalized such that

$$\int_{4\pi} d\omega \int_{-\infty}^{\infty} dE \, I_R(E, S_1) = f N_0 \,, \tag{2-22}$$

where $N_0$ is the source gamma ray intensity from the level of interest, $f$ is the source recoilless fraction, and $d\omega$ is the increment of fractional solid angle. With the geometry of Fig. 3 the energy distribution $I_R'(E, S_1)$ of the recoilless part of the scattered radiation is

$$I_R'(E, S_1) = \frac{f' W(\theta)}{1 + \alpha} \, d\omega \, d\omega' \mu(E) \, I_R(E, S_1) \frac{1}{\sin \gamma_1} \int_0^t d\eta \, e^{-\eta[\mu_e + \mu(E)][\csc \gamma_1 + \csc \gamma_2]} \,. \tag{2-23}$$

By performing the integration over $\eta$ we have

$$I_R'(E, S_1) = \frac{f' W(\theta)}{1 + \alpha} \, d\omega \, d\omega' \mu(E) \, I_R(E, S_1) \frac{1 - e^{-t[\mu_e + \mu(E)][\csc \gamma_1 + \csc \gamma_2]}}{(1 + \sin \gamma_1 \csc \gamma_2)[\mu_e + \mu(E)]} \,. \tag{2-24}$$

The intensities $N_R'(S_1)$ and $N_{NR}'(S_1)$ of gamma rays which are scattered into the fractional solid angle $d\omega'$ without and with recoil energy loss are, respectively,

$$N_R'(S_1) = \int_{-\infty}^{\infty} dE \, I_R'(E, S_1) = \frac{f' W(\theta)}{1 + \alpha} \, d\omega \, d\omega' \int_{-\infty}^{\infty} dE \, I_R(E, S_1) \mu(E)$$
$$\times \frac{1 - e^{-t[\mu_e + \mu(E)][\csc \gamma_1 + \csc \gamma_2]}}{(1 + \sin \gamma_1 \csc \gamma_2)[\mu_e + \mu(E)]} \tag{2-25}$$

and

$$N_{NR}'(S_1) = \frac{(1 - f') W(\theta)}{1 + \alpha} \, d\omega \, d\omega' \int_{-\infty}^{\infty} dE \, I_R(E, S_1) \mu(E)$$
$$\times \frac{1 - e^{-t[\mu_e(\csc \gamma_1 + \csc \gamma_2) + \mu(E) \csc \gamma_1]}}{\mu_e(1 + \sin \gamma_1 \csc \gamma_2) + \mu(E)} \,. \tag{2-26}$$
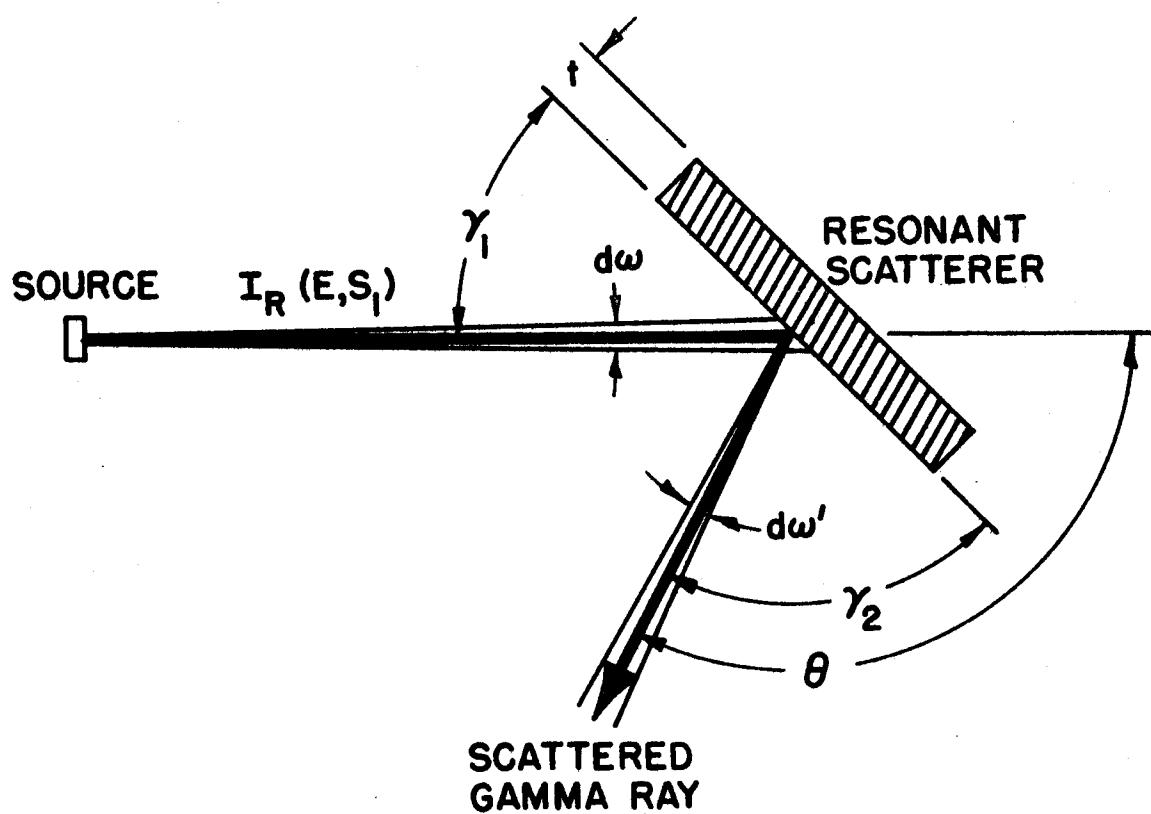
**Fig. 3.** The scattering geometry. The angles $\gamma_1$ and $\gamma_2$ and the thickness t are defined in the scattering plane. The scattering angle $\theta$ is equal to $\gamma_1 + \gamma_2$.

As indicated in Fig. 3 the scattering angle $\theta$ is the sum of the two angles $\gamma_1$ and $\gamma_2$ which are defined in the scattering plane. The thickness t of the scatterer is also defined in the scattering plane.

If the scatterer is thin, it is unlikely that a scattered gamma ray will be reabsorbed in the scattering foil. In this limit, $t(\mu_e + \mu(E)) \ll 1$, we have the relationships,

$$N_R'(S_1) = \frac{f' W(\theta) \, t \, d\omega \, d\omega'}{(1+\alpha) \sin\gamma_1} \int_{-\infty}^{\infty} dE \, I_R(E, S_1) \mu(E), \qquad (2\text{-}27)$$

$$N_{NR}'(S_1) = \frac{(1-f') W(\theta) \, t \, d\omega \, d\omega'}{(1+\alpha) \sin\gamma_1} \int_{-\infty}^{\infty} dE \, I_R(E, S_1) \mu(E), \qquad (2\text{-}28)$$

and

$$\frac{N_R'(S_1)}{N_{NR}'(S_1)} = \frac{f'}{(1-f')}. \qquad (2\text{-}29)$$

If one assumes the Lorentzian distributions Eq. (2-19) for the scatterer and

$$I_R(E, S_1) = \frac{2}{\pi \Gamma} \frac{N_0 f}{1 + \left[ 2/\Gamma (E - S_1) \right]^2}, \qquad (2\text{-}30)$$

for the source, the integral in Eqs. (2-27) and (2-28) has the value

$$\int_{-\infty}^{\infty} dE \, I_R(E, S_1) \mu(E) = f N_0 \mu_n \frac{\Gamma'}{\Gamma' + \Gamma} \frac{1}{1 + \left[ 2 S_1 / (\Gamma' + \Gamma) \right]^2}. \qquad (2\text{-}31)$$

Here $\Gamma$ and $\Gamma'$ are the source and scatterer widths, and $\mu_n$ is the resonance absorption coefficient at resonance

$$\mathcal{M}_n = f' \eta \sigma_o.$$ 

(2-32)

If the scatterer is not thin the exponentials in Eqs. (2-25) and (2-26) cannot be so easily approximated. By inserting the Lorentzian distributions, Eqs. (2-19) and (2-30), into (2-25) and (2-26) we have

$$N_R'(S_1) = \frac{ff'W(\theta) N_0 \, d\omega \, d\omega'}{(1+\alpha)} \frac{F\left(\frac{2}{\Gamma'}S_1, \beta_R\right) A, \Gamma/\Gamma')}{(1+\sin\gamma_1 \, \cosec\gamma_2)}$$

(2-33)

and

$$N_{NR}'(S_1) = \frac{f(1-f') W(\theta) N_0 \, d\omega \, d\omega'}{(1+\alpha)} F\left(\frac{2}{\Gamma'}S_1, \beta_{NR}\right) A, \Gamma/\Gamma').$$

(2-34)

Here the following quantities have been introduced:

$$\beta_R^2 = 1 + \mathcal{M}_n/\mathcal{M}_e,$$

$$\beta_{NR}^2 = 1 + \frac{\mathcal{M}_n/\mathcal{M}_e}{(1 + \sin\gamma_1 \, \cosec\gamma_2)},$$

(2-35)

$$A = \mathcal{M}_e t (\cosec\gamma_1 + \cosec\gamma_2).$$

The parameters of the scatterer are contained in the scattering function

$$F(x, \lambda, A, \Gamma/\Gamma') = \frac{(\lambda^2-1)}{\Gamma'/\Gamma} \frac{1}{\pi} \int_{-\infty}^{\infty} dy \frac{1 - e^{-A\left(\frac{\lambda^2+y^2}{1+y^2}\right)}}{[(\Gamma/\Gamma')^2 + (y-x)^2][\lambda^2 + y^2]},$$

(2-36)

where we have substituted x for $2S_1/\Gamma'$, y for $2E/\Gamma'$, and $\lambda$ for $\beta_R$ or $\beta_{NR}$.

For the case of a thick scatterer it is useful to define a function

$$\epsilon(x, \lambda, A, \Gamma/\Gamma') = \frac{\int_{-\infty}^{\infty} dy \frac{e^{-A\left(\frac{\lambda^2 + y^2}{1 + y^2}\right)}}{[(\Gamma/\Gamma')^2 + (y-x)^2][\lambda^2 + y^2]}}{\int_{-\infty}^{\infty} \frac{dy}{[(\Gamma/\Gamma')^2 + (y-x)^2][\lambda^2 + y^2]}} \qquad (2\text{-}37)$$

which tends to zero for large values of the quantity

$$A(\lambda^2 + x^2)/(1 + x^2).$$

Equation (2-36) can then be written in the form

$$F(\frac{2}{\Gamma}S_1, \lambda, A, \Gamma/\Gamma') = \frac{(\lambda^2 - 1)[1 - \epsilon(\frac{2}{\Gamma}S_1, \lambda, A, \Gamma/\Gamma')]}{\lambda(\lambda + \Gamma/\Gamma')[1 + \{2S_1/(\lambda\Gamma' + \Gamma)\}^2]} \qquad (2\text{-}38)$$

where the Lorentzian dependence on the Doppler shift is explicitly shown. Computer evaluations of $F(0, \lambda, A, \Gamma/\Gamma')$ and $\epsilon(0, \lambda, A, \Gamma/\Gamma')$ have been carried out and the results are shown in Figs. 4-9.

## 2.4 Determination of the Recoilless Fraction from the Total Resonant Scattering

The total resonant scattering on resonance,

$$N_T'(0) = N_R'(0) + N_{NR}'(0), \qquad (2\text{-}39)$$

can be measured by comparing the scattered count rate on and off resonance.

Inserting Eqs. (2-33) and (2-34) we obtain

$$N_T'(0) = \frac{N_0 \, d\omega \, d\omega' \, W(\theta)}{1 + \alpha} \, f\left[\frac{f' F(0, \beta_R, A, \Gamma/\Gamma')}{1 + \sin\gamma_1 \, \text{cosec}\,\gamma_2} + (1 - f') F(0, \beta_{NR}, A, \Gamma/\Gamma')\right]$$

(2-40)

If the solid angles involved are not small, appropriate averages must be made.

In most cases of interest, f' is small so that

$$N_T'(0) \approx \frac{N_0 \, d\omega \, d\omega' \, W(\theta)}{(1 + \alpha)} \, f \, F(0, \beta_{NR}, A, \Gamma/\Gamma')$$

(2-41)

Usually $\alpha$ and $W(\theta)$ are known and from the measured values of $N_T'(0)$ and $N_0$ one can determine the product $f \, F(0, \beta_{NR}, A, \Gamma/\Gamma')$. If $f$, $\mu_e$, $t$, $\sigma_0$, $n$, and $\Gamma/\Gamma'$ are known, the curves of F plotted in Figs. 4-9 and Eqs. (2-32) and (2-33) can be used to obtain a unique value for f'.

Fig. 4. The functions $F(0,\lambda,A,\Gamma/\Gamma')$ and $\epsilon(0,\lambda,A,\Gamma/\Gamma')$ defined in Eqs. (2-36) and (2-37) respectively are given as a function of $\lambda$ for various values of A and for $(\Gamma/\Gamma')^2 = 0.2$.

$F(o,\lambda,A,.447)$

$\epsilon(o,\lambda,A,.447)$

$\left(\dfrac{\Gamma}{\Gamma'}\right)^2 = 0.2$

$A = \mu_e t(\csc \gamma_1 + \csc \gamma_2) = 4.0$

$A = 0.1$

$\lambda^2$

Fig. 5. The functions $F(0,\lambda,A,\Gamma/\Gamma')$ and $\in(0,\lambda,A,\Gamma/\Gamma')$ defined in Eqs. (2-36) and (2-37) respectively are given as a function of $\lambda$ for various values of A and for $(\Gamma/\Gamma')^2 = 0.8$.

Fig. 6. The functions $F(0,\lambda,A,\Gamma/\Gamma')$ and $\epsilon(0,\lambda,A,\Gamma/\Gamma')$ defined in Eqs. (2-36) and 2-37) respectively are given as a function of $\lambda$ for various values of A and for $(\Gamma/\Gamma')^2 = 1.0$.

$F(0,\lambda,A,1.0)$
$\epsilon(0,\lambda,A,1.0)$
$\left(\dfrac{\Gamma}{\Gamma^1}\right)^2 = 1.0$

$A = 0.1$

$0.2$

$0.4$

$1.0$

$A = \mu e^{\dagger}(\cosec\,\gamma_1 + \cosec\,\gamma_2) = 4.0$

$1.0$

$0.4$

$0.2$

$0.1$

$4.0$

$\lambda^2$
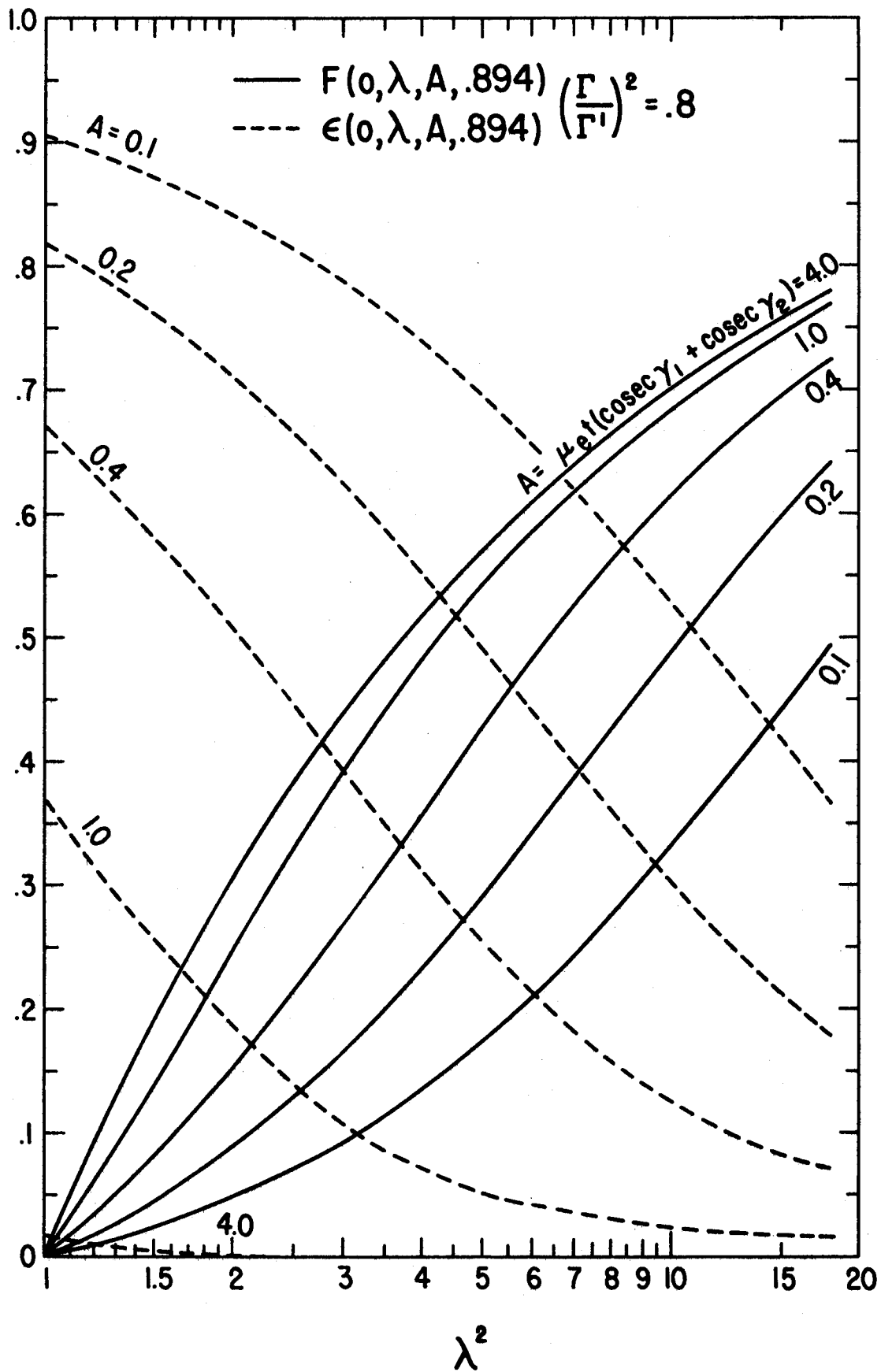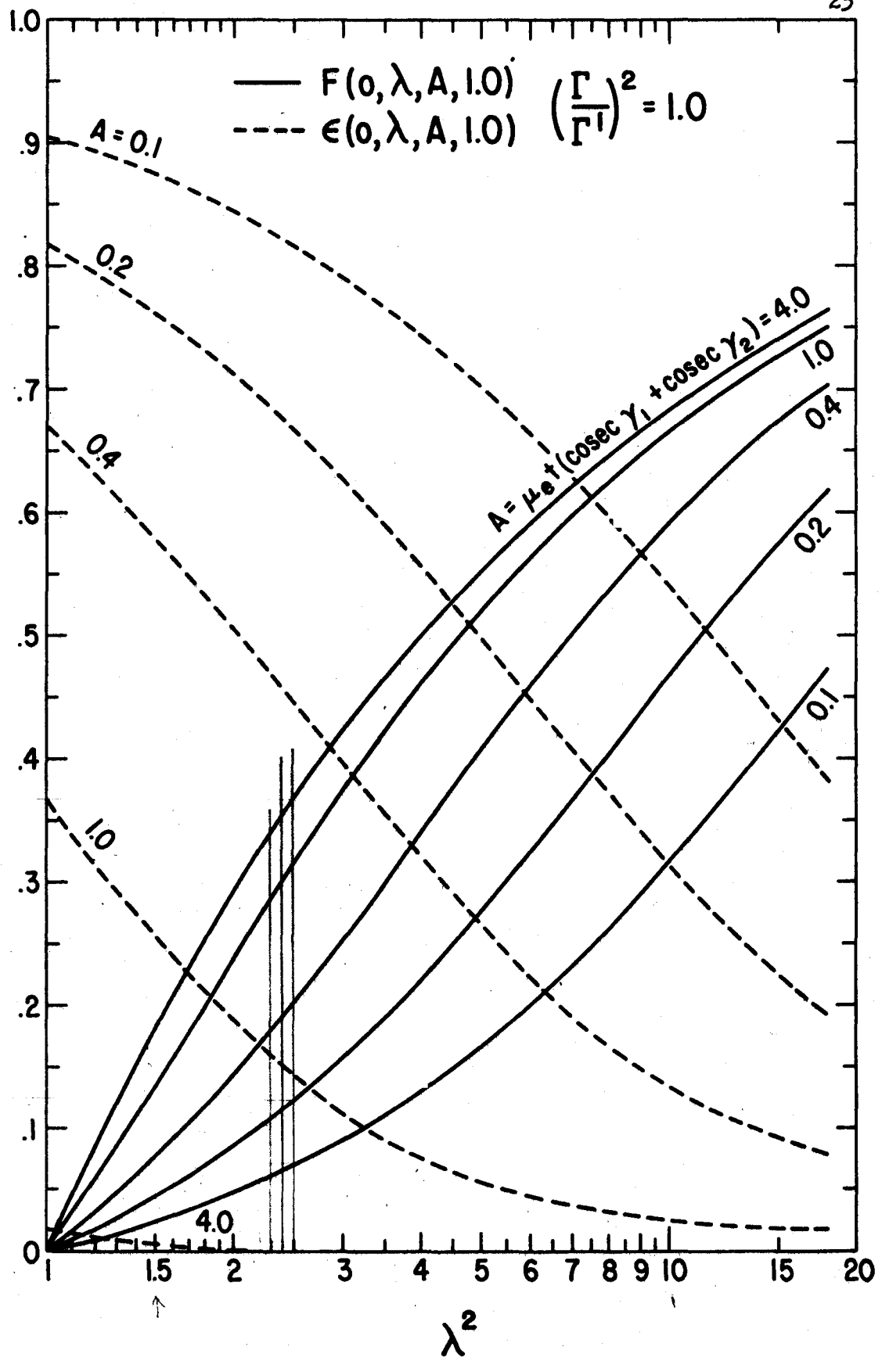
Fig. 7. The functions $F(0,\lambda,A,\Gamma/\Gamma')$ and $\xi(0,\lambda,A,\Gamma/\Gamma')$ defined
in Eqs. (2-36) and 2-37) respectively are given as a
function of $\lambda$ for various values of A and for $(\Gamma/\Gamma')^2 = 1.2$.
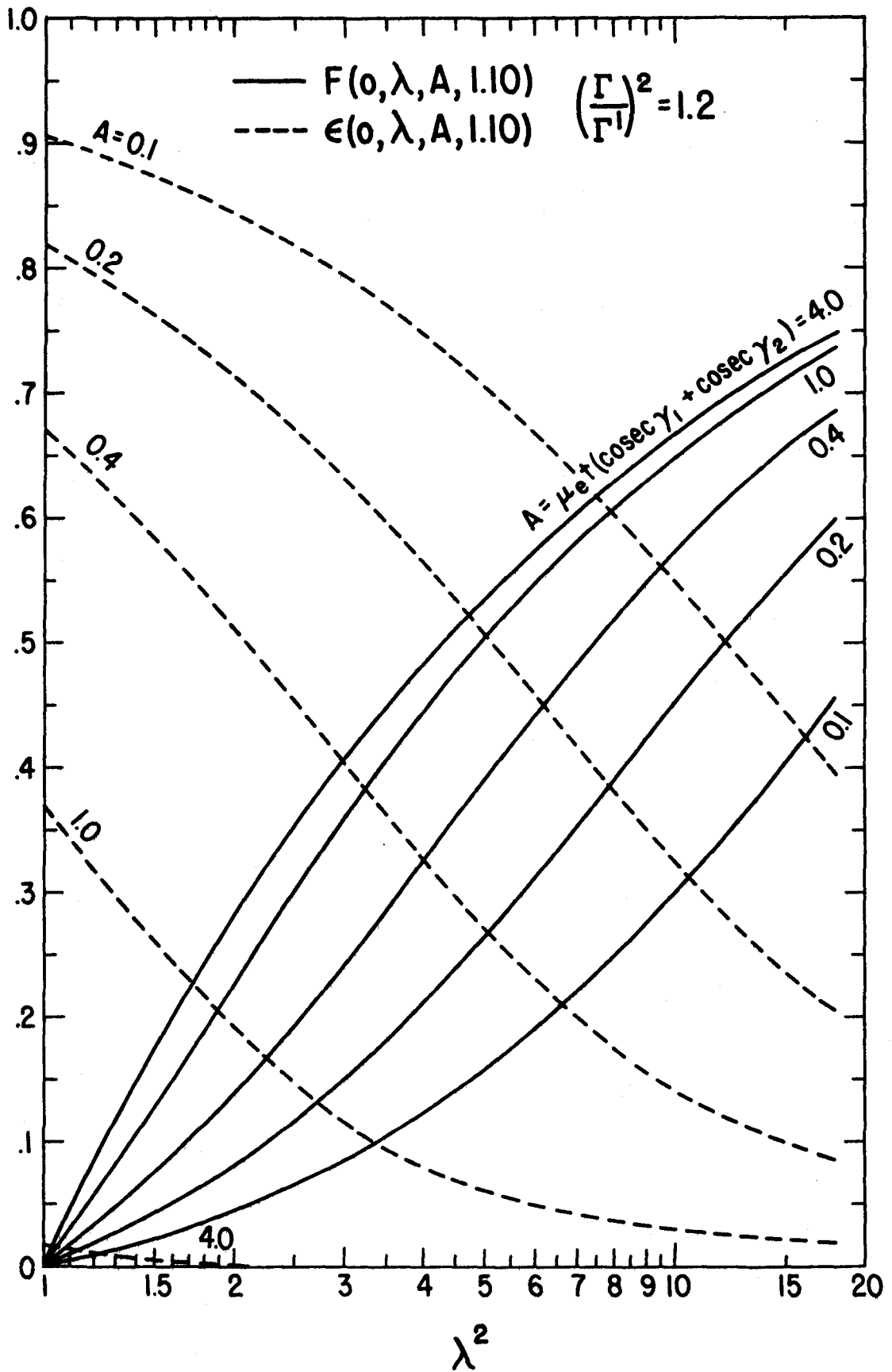
Fig. 8.  The functions $F(0,\lambda,A,\Gamma/\Gamma')$ and $\epsilon(0,\lambda,A,\Gamma/\Gamma')$ defined
in Eqs. (2-36) and (2-37) respectively are given as a
function of $\lambda$ for various values of A and $(\Gamma/\Gamma')^2 = 2.0$.
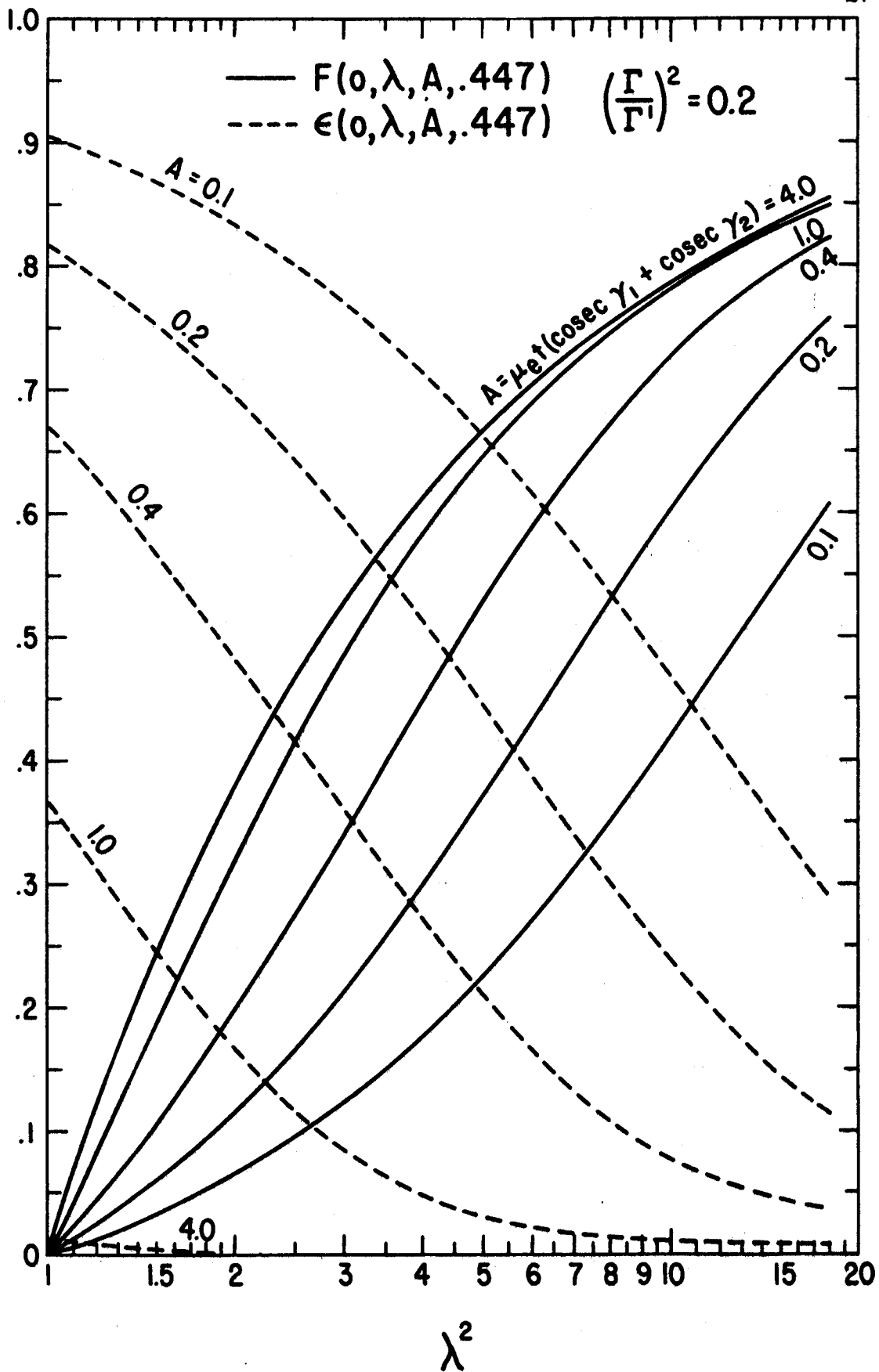
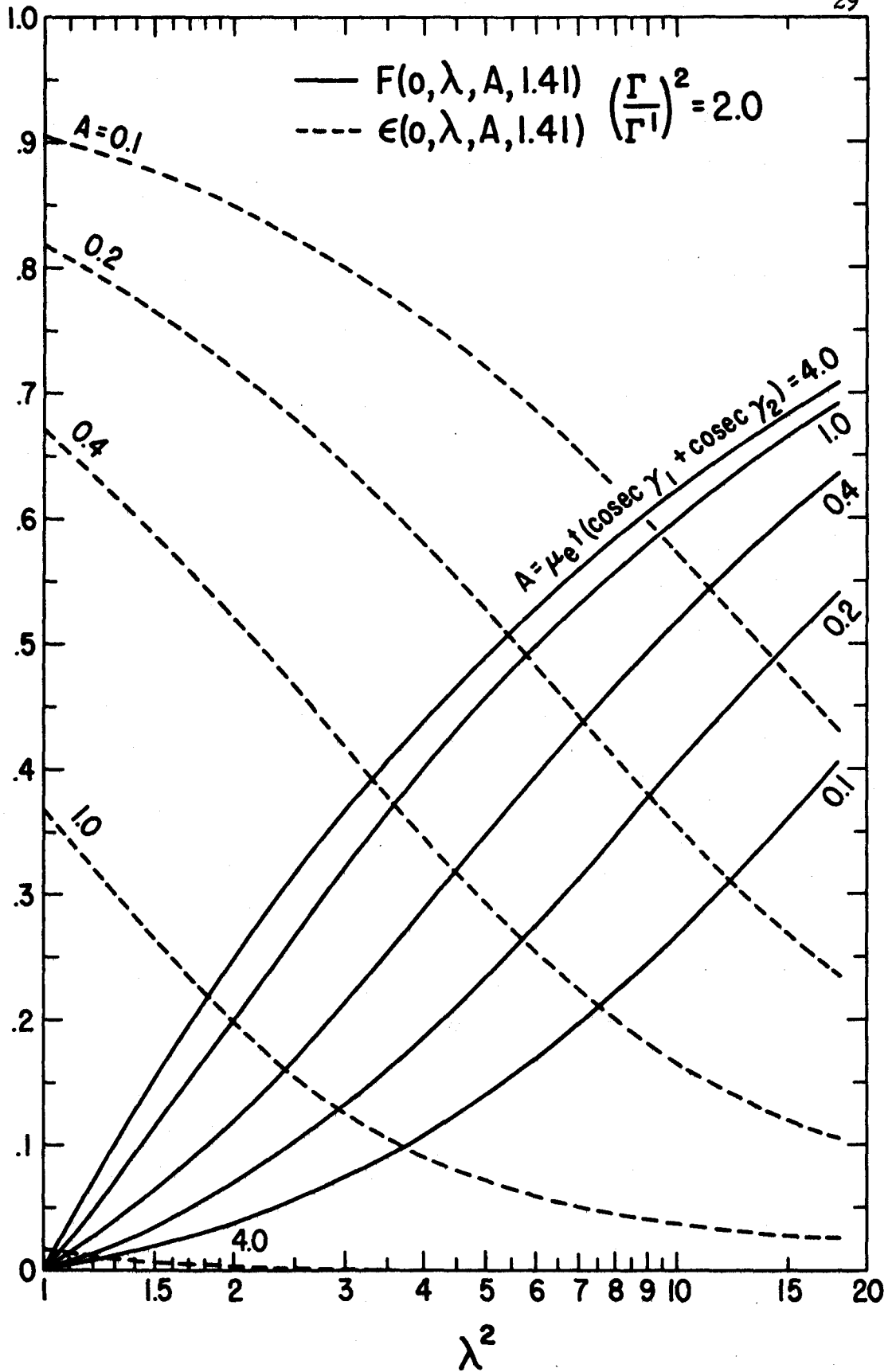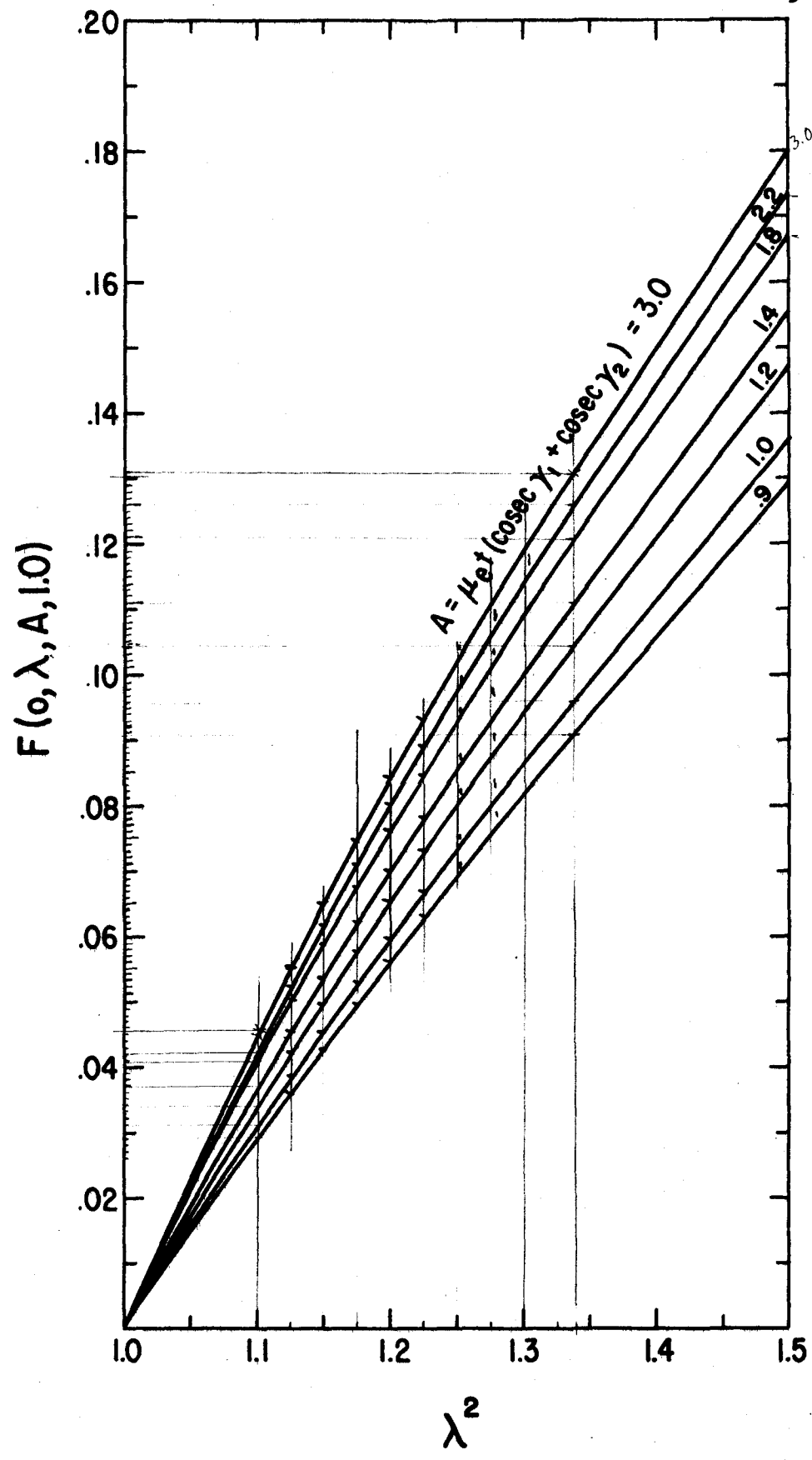Fig. 9.  The scattering function $F(0,\lambda,A,\Gamma/\Gamma')$ versus $\lambda$ for
$\Gamma/\Gamma' = 1$ and various values of A.

$A = \mu_e t (\text{cosec } \gamma_1 + \text{cosec } \gamma_2) = 3.0$

3.0

2.2

1.8

1.4

1.2

1.0

.9

$F(o, \lambda, A, 1.0)$

$\lambda^2$

# 3. EXPERIMENTAL PROCEDURE

The experimental arrangement (Fig. 10) was specifically designed for the observation of Mössbauer effects with high transition energies $E_\gamma$ and small recoilless fractions. The backscattering geometry was chosen to minimize B, the background caused by nonresonant processes. Large solid angles and cold source and scatterer temperatures were used to obtain the highest possible resonant scattering intensity $N_T^!(0)$. The main objective of the experimental design was to obtain large signal to noise ratios $N_T^!(0)/B$ and high count rates for experiments with small recoilless fractions.

The Mössbauer effects were observed by measuring the resonant scattering of the recoillessly emitted gamma rays as a function of the scatterer velocity. The intensity of the resonant scattering

$$N_T^{'}(0) \sim \frac{f}{1+\alpha} N_0 \, \Delta\omega \, \Delta\omega' \, \overline{W(\theta)} \, \overline{F(0, \beta_{NR}, A, \Gamma/\Gamma')} , \qquad (3\text{-}1)$$

was determined from the count rate in the peak of the curve of the scattered intensities versus scatterer velocity. In this expression

$\overline{W(\theta)}$ and $\overline{F(0, \beta_{NR}, A, \Gamma/\Gamma')}$ are average values of the angular correlation and scattering functions, and $\Delta\omega$ and $\Delta\omega'$ are the solid angles subtended by the scatterer and the counter respectively.

## 3.1 Nonresonant Background

For the Mössbauer transitions energies of these experiments the background counting rate was mainly caused by the following processes:

Fig. 10. Experimental arrangement. Source and scatterer are in thermal contact with a liquid helium reservoir in an evacuated cryostat. The tungsten shield carrying the source is supported from the helium container by three thin wall tubes, two of which serve as a drip tube. The scatterer cone is suspended from the velocity transducer on top of the cryostat by a drive rod, the upper part of which is a thermal insulator, whereas the lower part made of aluminum is in thermal contact with the helium container through a strip of soft copper. The velocity transducer consists of two mechanically coupled coils moving in the field of a loudspeaker type magnet, with one of the coils acting as a drive, the other one as a pickup. The radiation shield connected to the liquid nitrogen container is lined with lead on the inside to reduce the background counting rate due to Compton scattering. The source and scatterer temperatures are measured by two platinum resistors not shown in the figure. One of them is cemented to the scatterer cone and the other one is in a hole drilled through the tungsten shield. The scintillation counter, a 1-1/2" x 1/2" NaI(TI) Integral Line assembly, is kept at room temperature.

Magnet Drive

Liquid Nitrogen

Liquid Helium

Drip Tube

Lead Shield

Scintillation Counter

To Diffusion Pump

Drive Rod (Bakelite or Pyrex Tube)

Copper Strip Scatterer

Source

Tungsten Shield

0 1 2 3 4"
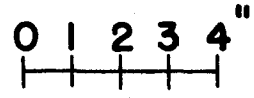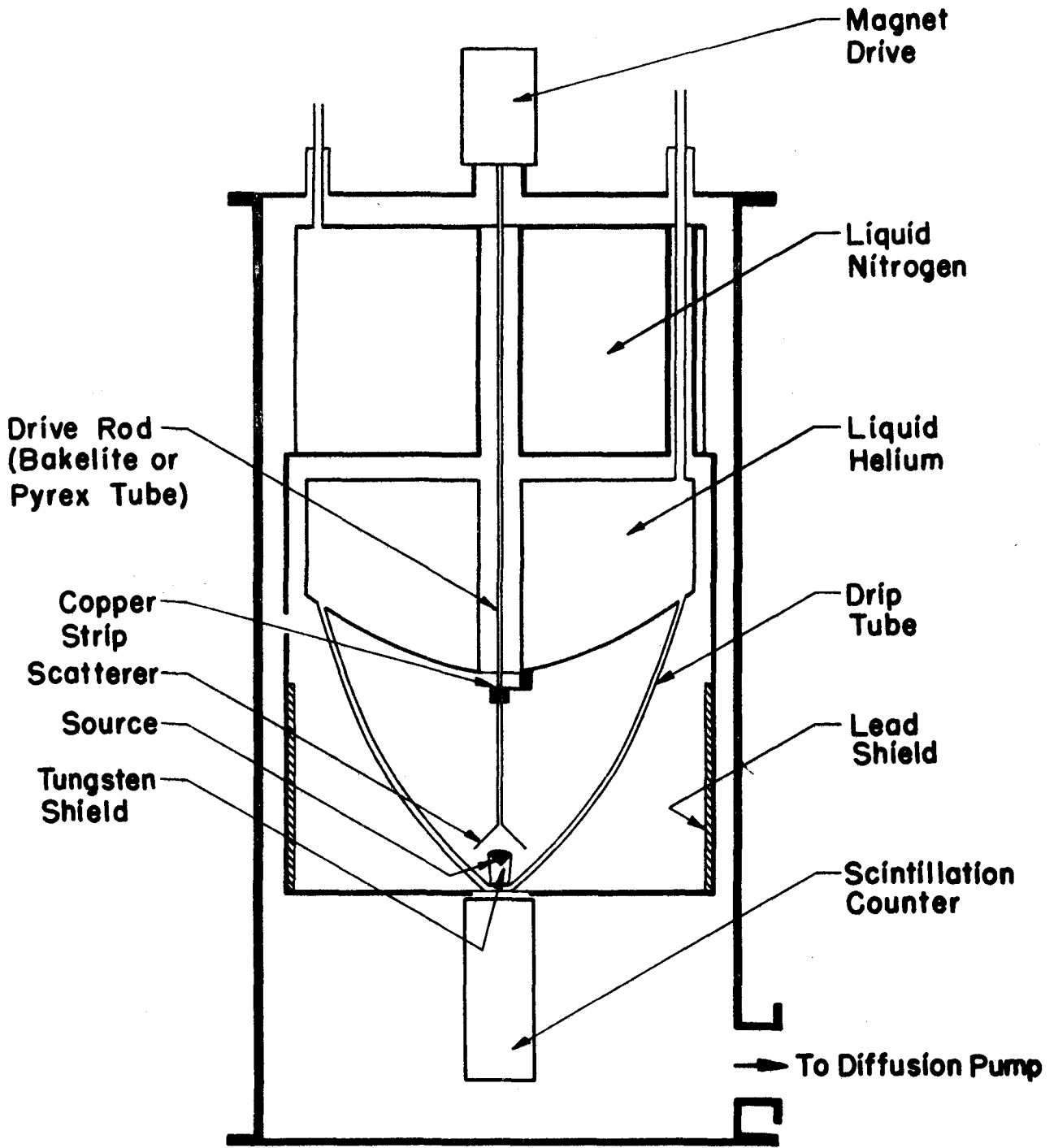
a.  Compton scattering by the scatterer of the gamma rays from the level $E_\gamma$.

b.  Compton scattering of higher energy gamma rays and Bremstrahlung by the scatterer.

c.  Compton scattering from parts of the apparatus.

d.  Creation of Bremstrahlung by beta particles which strike the scatterer.

e.  Incomplete shielding of the counter from direct radiation from the source.

The background caused by the first process was greatly reduced by using the back scattering geometry shown in Fig. 11. For transition energies $E_\gamma \gtrsim 100$ keV and large angles $\theta$ the Compton scattered gamma rays have a sufficiently lower energy,

$$E_C = \frac{E_\gamma}{1 + \frac{E_\gamma}{mc^2}(1 - \cos\theta)})$$  (3-2)

to be resolved from the resonantly scattered energy $E_\gamma$ with a scintillation counter. Here $mc^2$ is the rest energy of the electron. The importance of this Compton shift can be seen from Fig. 12 where the scattered spectrum of the $Sm^{153}$ source is shown. By setting the pulse height selector channel on the upper half of the 103 keV peak of the direct source spectrum the Compton scattering of the 103 keV gamma rays can be almost completely avoided.

Backscattering has an additional advantage for experiments with the even-even nuclei $Os^{186}$ and $Os^{188}$, where the spin of the ground and first rotational levels are $0^+$ and $2^+$ respectively. The scattered intensity is enhanced in the forward and backward directions as a result of the strong angular correlation.

Fig. 11.  The cylindrically symmetric scattering geometry.  The
          source is fixed on the bottom of the cone-shaped cup
          of the tungsten shield.  On top of the source is a
          graphite disc which stops all the beta particles.  The
          graphite is covered by an aluminum foil acting as a
          radiation shield.  The scattering material is cemented
          to the entire inner surface of the aluminum cone to
          obtain a large solid angle, or to a ring-shaped portion
          of the surface defined by angles $\psi_1$ and $\psi_2$ to obtain
          a better velocity resolution.

Aluminum Rod

Aluminum Cone
.006 Thick

Scatterer
185 mg /cm$^2$
Osmium Metal

Graphite Disc

50°

$\psi_1$

$\psi_2$

Source

Tungsten Shield
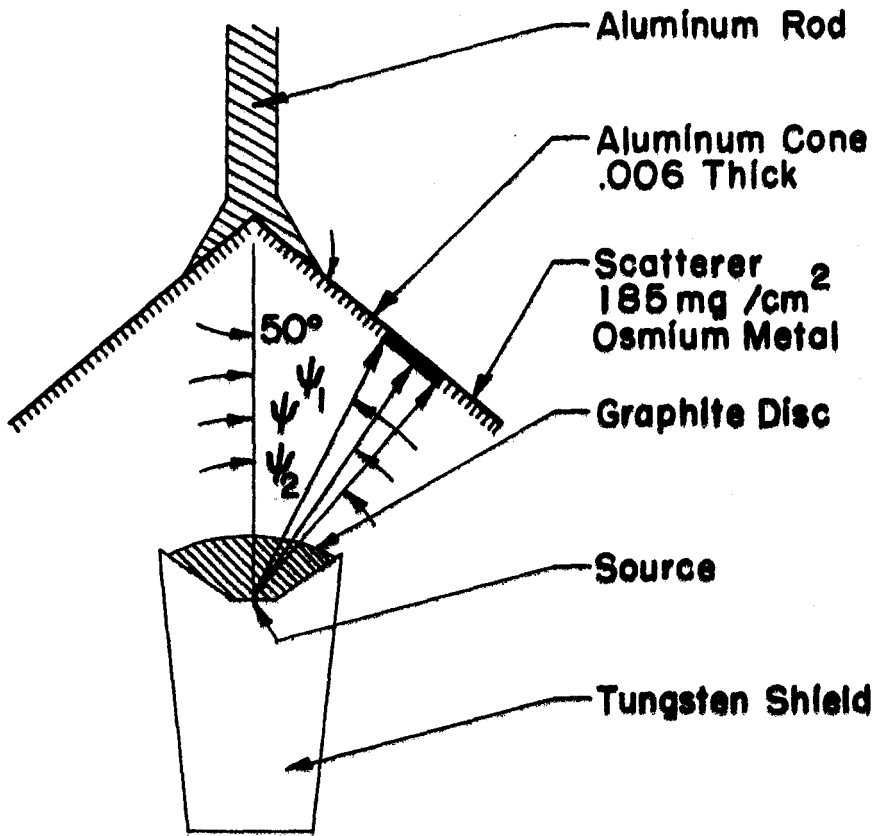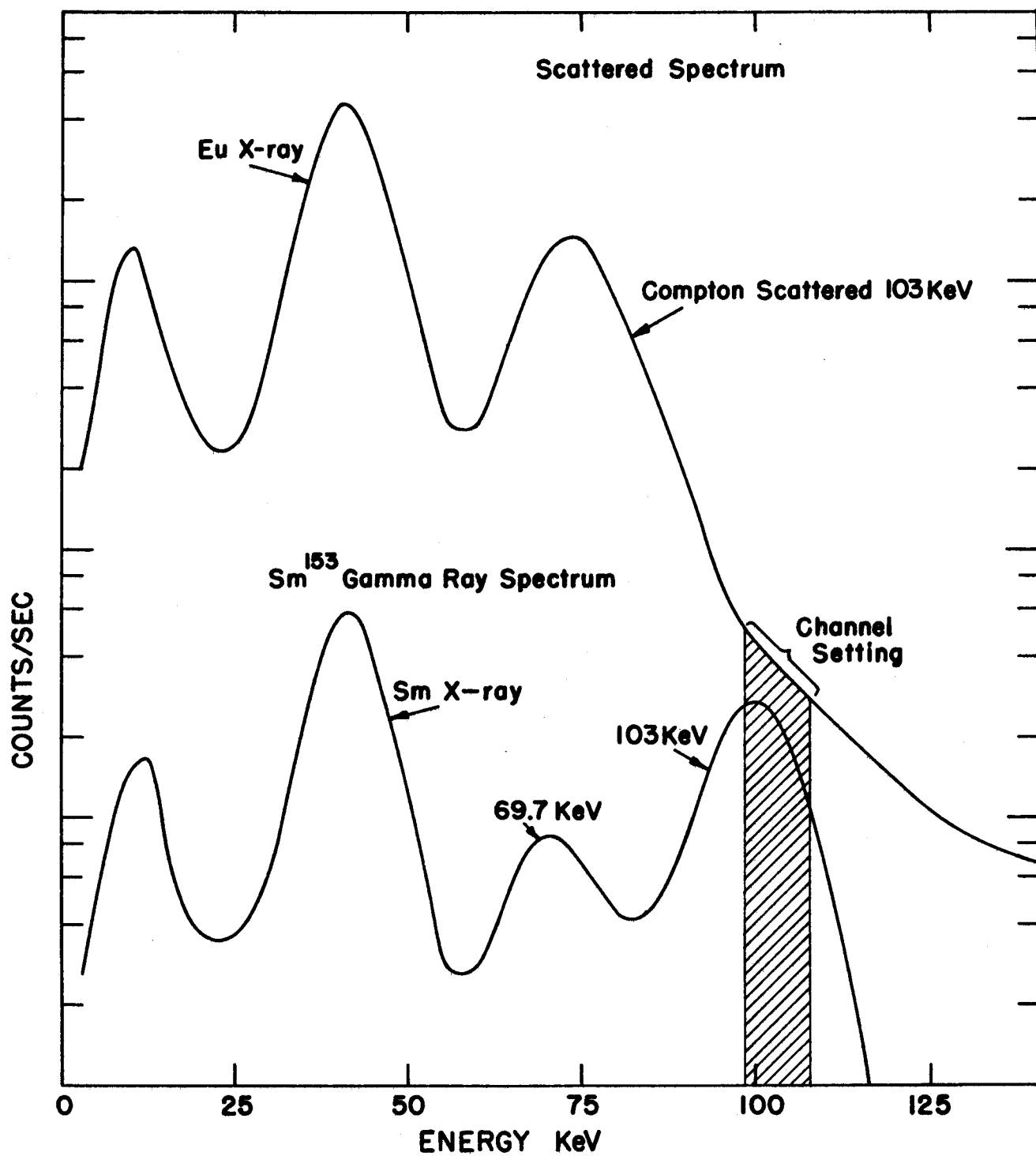
NaI(Tl) Crystal
(1 1/2 × 1/2)

1"

Fig. 12. The scintillation counter spectrum of the scattered
and direct gamma rays from a $Sm^{153}$ source. The con-
tribution to the scattered count rate in the 103 keV
channel from the Compton scattered 103 keV gamma rays
is small because of the large Compton shift.

$$W(\theta) = 1 + 0.3571 \, P_2(\cos\theta) + 1.143 \, P_4(\cos\theta),$$

for the spin sequence $0 \rightarrow 2 \rightarrow 0$.

In order to avoid a large amount of Compton scattering of higher energy radiation[*] from the scatterer we chose sources which beta decayed predominantly to the level of interest or the ground state. The $Re^{188}$ source used in the $Os^{188}$ experiment had some higher energy gamma rays and internal Bremstrahlung which made a noticable contribution to the background.

Compton scattering from the apparatus was minimized by lining the inside of the cryostat with lead. The high-Z material was used because it had a high ratio of photoelectric absorption to Compton scattering cross sections for the troublesome energies.

The creation of Bremstrahlung in the scatterer was prevented by stopping the beta particles in the graphite disc. The low-Z material absorbed the electrons while producing a minimum of Bremstrahlung.

The counter was shielded from the direct source radiation by the tungsten block. The thickness of the block was adequate for the $Re^{188}$ source which had the highest energy radiations.

## 3.2 The Scatterer and the Scattering Geometry

The scatterer was made by cementing the powder containing the Mössbauer isotope to the scatterer support. The scatterer support was a thin cone and rod which was turned from one piece of aluminum.

---

[*] In many cases this part of the background can be eliminated by using two counters and counting the resonantly scattered gamma rays in coincidence with a preceeding radiation.

The cylindrically symmetric geometry makes it possible to have large scatterer and counter solid angles $\Delta\omega$ and $\Delta\omega'$. The large solid angles were used to obtain high count rates and to improve the ratio $N_T'(0)/B$. The latter effect was especially important for the $Os^{186}$ and $Os^{188}$ cases where a large part of the background resulted from contributions from "c" and "e" which are independent of the solid angle.

A large $\Delta\omega$, however, has a serious disadvantage for measurements of shifts and splittings. If the scatterer has a velocity v toward the source it will have a velocity component $-v\cos\psi$ in the direction of emission of a gamma ray emitted at an angle $\psi$ with the cylindrical axis. The Doppler shift of the source with respect to the scatterer is then $\quad S_\psi = \dfrac{v\cos\psi}{c}E_\gamma$ where c is the velocity of light. If the scatterer is made in the form of a symmetric ring defined by the maximum and minimum angles $\psi_2$ and $\psi_1$ the gamma rays emitted experience a range of Doppler shifts defined by $\cos\psi_1$ and $\cos\psi_2$. A calculation of the effect of this spread of Doppler shifts was carried out for the full scatterer defined by $\psi_1 = 0°$ and $\psi_2 = 52°$ for an unshifted source and scatterer of natural line shape. It showed that the curve of the scattered intensity versus v could be reasonably well approximated by a Lorentzian with a velocity scale given by $v_{eff} = v/1.3$.

The solid angle subtended by the scatterer for this case was 0.24 and the geometrical factor of Eq. (3-1), $\Delta\omega\Delta\omega'\ \overline{W(\theta)}$, had the value 1.5 x $10^{-3}$. Here $\overline{W(\theta)}$ is defined by

$$\Delta\omega\,\Delta\omega'\ \overline{W(\theta)} = \int_{\Delta\omega}d\omega \int_{\Delta\omega'}d\omega'\,W(\theta) \qquad (3\text{-}3)$$

This geometry was used for the $Os^{186}$ and $Os^{188}$ experiments where unshifted single lines were observed.

For the measurements of shifts and splittings where distributions other than unshifted single lines were involved a smaller $\Delta\omega$ was used where $\psi_1$ and $\psi_2$ had the values $31°$ and $40°$ respectively.


## 3.3 The Scatterer Motion

The velocity of the scatterer was provided and measured by a two coil magnetic drive.[*] The scatterer was attached to the magnetic drive by means of a drive rod (bakelite or pyrex tube). A signal proportional to the scatterer velocity was furnished by the pick up coil of the magnet drive. The sinusoidal motion of the scatterer was checked and calibrated by means of an $Fe^{57}$ Mössbauer experiment. A $Co^{57}$ in iron source was mounted on the scatterer and the transmission of the 14.4 keV gamma rays through an enriched iron absorber was measured. The well known hyperfine pattern was observed and was used to calibrate the pickup signal of the magnet drive in terms of the rod velocity. Vibrational broadening was checked for scatterer motions with maximum velocity up to $\pm$ 2.5 cm/sec. With the $\pm$ 2.5 cm/sec velocity amplitude displayed over 128 channels of the multi-channel analyzer the broadening was found to be less than the multichannel resolution and therefore negligible compared with the natural widths of the Mössbauer isotopes investigated.


## 3.4 Source and Scatterer Temperatures

The source and scatterer were cooled to obtain the largest possible recoilless fractions. The source was mounted on a tungsten block which served to shield the counter from direct gamma rays. The block was in

---

[*]The magnet drive was made by M. Atac and is similar to one described by Kankeleit.[23]

thermal contact with a drip tube from the liquid helium vessel. The exhaust end of the drip tube passed through the liquid helium and nitrogen vessels and was open to the atmosphere. By closing this end and heating the tungsten block the source temperature could be adjusted. A platinum resistor was cemented in a hole in the tungsten block and was used to measure the source temperature.

The scatterer was cooled to $30^\circ$K by conduction to the liquid helium vessel. The conduction path was through the aluminum scatterer support and a copper strip. The copper strip also served to stabilize the motion of the drive rod. The measurement of the scatterer temperature was made by means of a platinum resistor which was cemented to the conical part of the scatterer support.

Lower scatter temperatures, which were independent of the source temperature, were obtained by surrounding the scatterer with a thin copper and aluminum heat shield. The heat shield was attached to the helium vessel by means of three 1/8" copper rods.

## 3.5  Counting Equipment

A $1\frac{1}{2}$" x $\frac{1}{2}$" integral line scintillation counter assembly was used for the experiments. The gamma ray spectrum of $Sm^{153}$ is shown in Fig. 12. The corresponding spectrum of the scattered gamma rays is also shown, with the pulse height selector setting used in the experiment. The PHS setting was adjusted to obtain the best signal to noise ratio consistent with a high count rate.

The standard pulses from the pulse height selector were modulated by the velocity signal from the pickup coil of the magnet drive. The modulated pulses were then stored in either 64 or 128 channels of a 256 channel

analyzer and time normalized to give the scattered count rate vs. v. For the measurement of isomer shifts the pickup signal was periodically reversed. The shifts were then evaluated from the relative displacement of the two curves of the scattered count rate vs. v.

3.6 Sources and Scatterers

3.61 Sources and Scatterer for the Osmium Experiments. Sources were made by neutron irradiation of natural rhenium metal. The only radio isotopes produced were $Re^{186}$ and $Re^{188}$ with 90 and 17 hour half-lives. The $Os^{188}$ experiments were performed immediately after the irradiation to take advantage of the initial ratio of 5.6 for the intensities of the $Os^{188}$ and $Os^{186}$ transitions respectively. The $Re^{188}$ activity decayed quite rapidly so that after about a week a relatively uncontaminated $Re^{186}$ source remained.

The scatterer consisted of a 185 mg/cm$^2$ layer of natural osmium containing 1.6% $Os^{186}$ and 13.3% $Os^{188}$. The metallic osmium powder was cemented to the entire inner surface of the scatterer support.

3.62 $Sm^{153}$ Sources and $Eu^{153}$ Scatterers. The 103 keV level of $Eu^{153}$ can be reached either by beta decay from $Sm^{153}$ or K-capture from $Gd^{153}$. The 47 hour $Sm^{153}$ was used because the 103 keV gamma ray has a higher branching ratio when fed by this parent. The sources used were in the chemical forms $Sm_2O_3$ and $SmF_3$. The $Sm_2O_3$ sources were made by neutron irradiation of $Sm_2O_3$ powder. Neither the oxygen nor other samarium isotopes caused serious radioactive contamination. Since the neutron activation cross sections of fluorine are quite large the fluoride source was made after the samarium had been irradiated. Natural europium which has an

$Eu^{153}$ abundance of 52.18% was used as a scatterer for all the experiments. The chemical forms $Eu_2O_3$ and europium iron garnet ($5Fe_2O_3 \cdot 3Eu_2O_3$) were used.


    3.63  $\underline{Ce^{141} \text{ Sources and the } Pr^{141} \text{ Scatterer}}$. The 145 keV level of $Pr^{141}$ is fed by the beta decay of $Ce^{141}$. The cerium sources which had a radioactive contamination of about one percent were purchased from Nuclear Science and Engineering Corp.[*] The atomic configuration of cerium, $6s^2 4f^2$ makes it possible to form $4^+$ compounds. Sources were made in the chemical forms $CeO_2$ ($4^+$) and $CeF_3$ ($3^+$).

    Natural praseodymium which has a 100% abundance of $Pr^{141}$ was used as the scatterer. The chemical form was $Pr_6O_{11}$ ($Pr_2O_3 \cdot 4PrO_2$).

---

[*]Nuclear Science and Engineering Corp., Pittsburgh 36, Pa.

## 4. MÖSSBAUER SCATTERING WITH $Os^{186}$ AND $Os^{188}$

### 4.1 Experimental Results

The normalized scattered count rates for the two isotopes are shown as a function of $v_{eff}$ in Figs. 13 and 14. Single resonant peaks of 9.7% and 6.5% of the background level were observed for $Os^{186}$ and $Os^{188}$ with the source and scatterer at $26^{\circ}$ K and $30^{\circ}$ K respectively. The observed peaks were fitted to a Lorentzian curve and were found to have widths that were larger by factors of $1.24 \pm 0.08$ and $1.37 \pm 0.09$ than the widths corresponding to the half-lives 0.84 nsec[24] and 0.71 nsec[25] for $Os^{186}$ and $Os^{188}$ respectively. Isomer shifts were observed to be less than 0.04 of the experimental line width for both isotopes. During these runs data was also taken with the source and scatterer temperatures $82.5^{\circ}$ K and $79^{\circ}$ K. The sets of data for both isotopes were taken with the same scatterer and the same geometry.

The source strength for the Mössbauer transition was measured before each run with the scintillation counter that was used in the experiments. Typical source strengths were $5.7 \ 10^{7}$ gamma rays per sec. With this source strength the total scattered count rate for $Re^{186}$ was 320 counts/sec. Scattered count rates with $Re^{188}$ were higher as a result of the three times larger background.

With the measured values of the resonantly scattered intensities and source strengths and the calculated value for the geometrical factor $\Delta\omega \ \Delta\omega' \ \overline{W(\theta)}$ we used Eq. (3-1) to obtain the values for the reduced intensity,

$$\frac{N_T'(0)}{N_0 \ \Delta\omega \ \Delta\omega' \ \overline{W(\theta)}} = \frac{f \ \overline{F(0, \lambda, A, \Gamma/\Gamma')}}{1 + \alpha} \qquad (4-1)$$
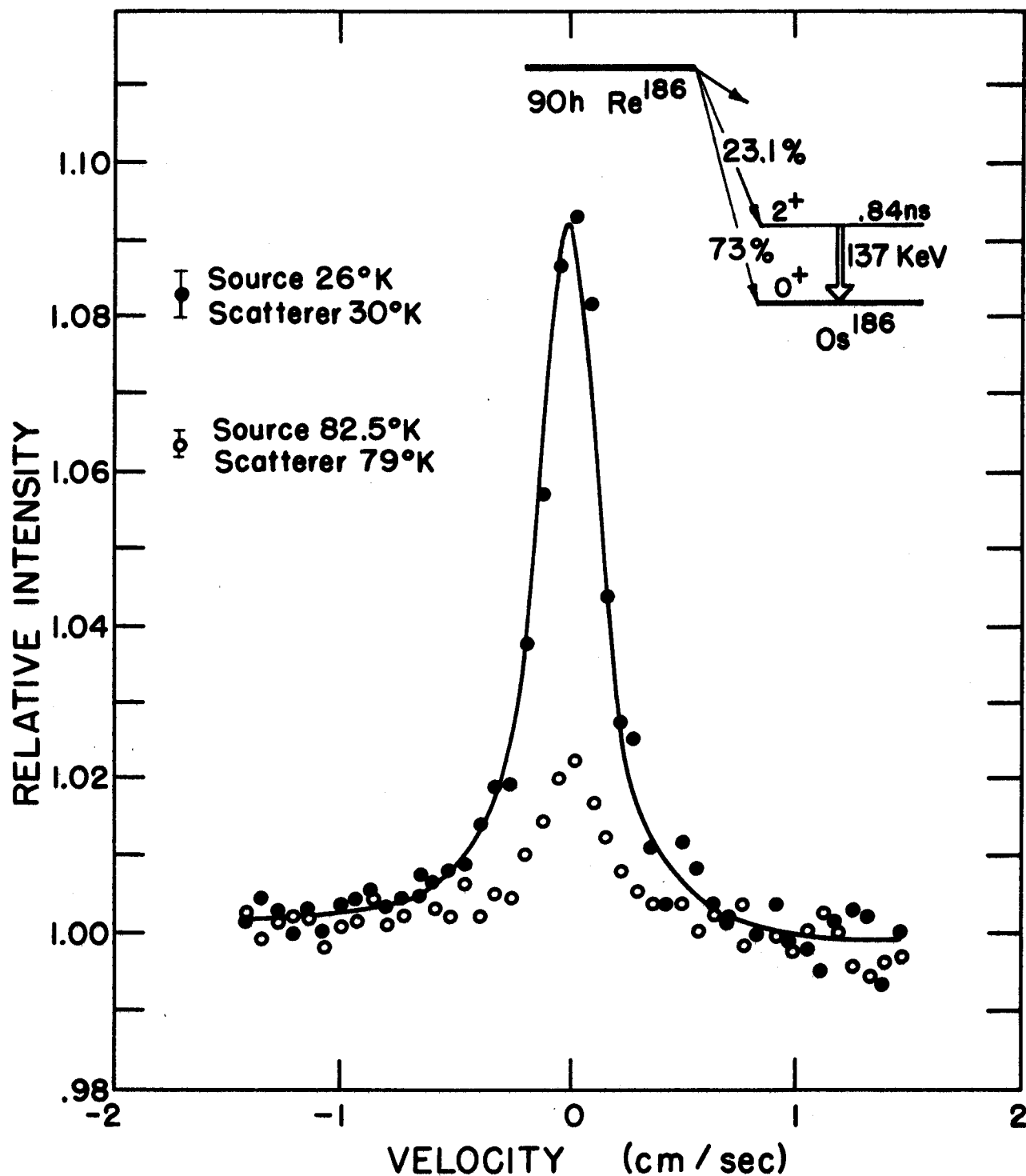
given in table 1.

Fig. 13. The scattered count rate for the 137 keV transition of Os[186] as a function of the effective scatterer velocity, which is given by the rod velocity divided by 1.3. The background is normalized to 1.
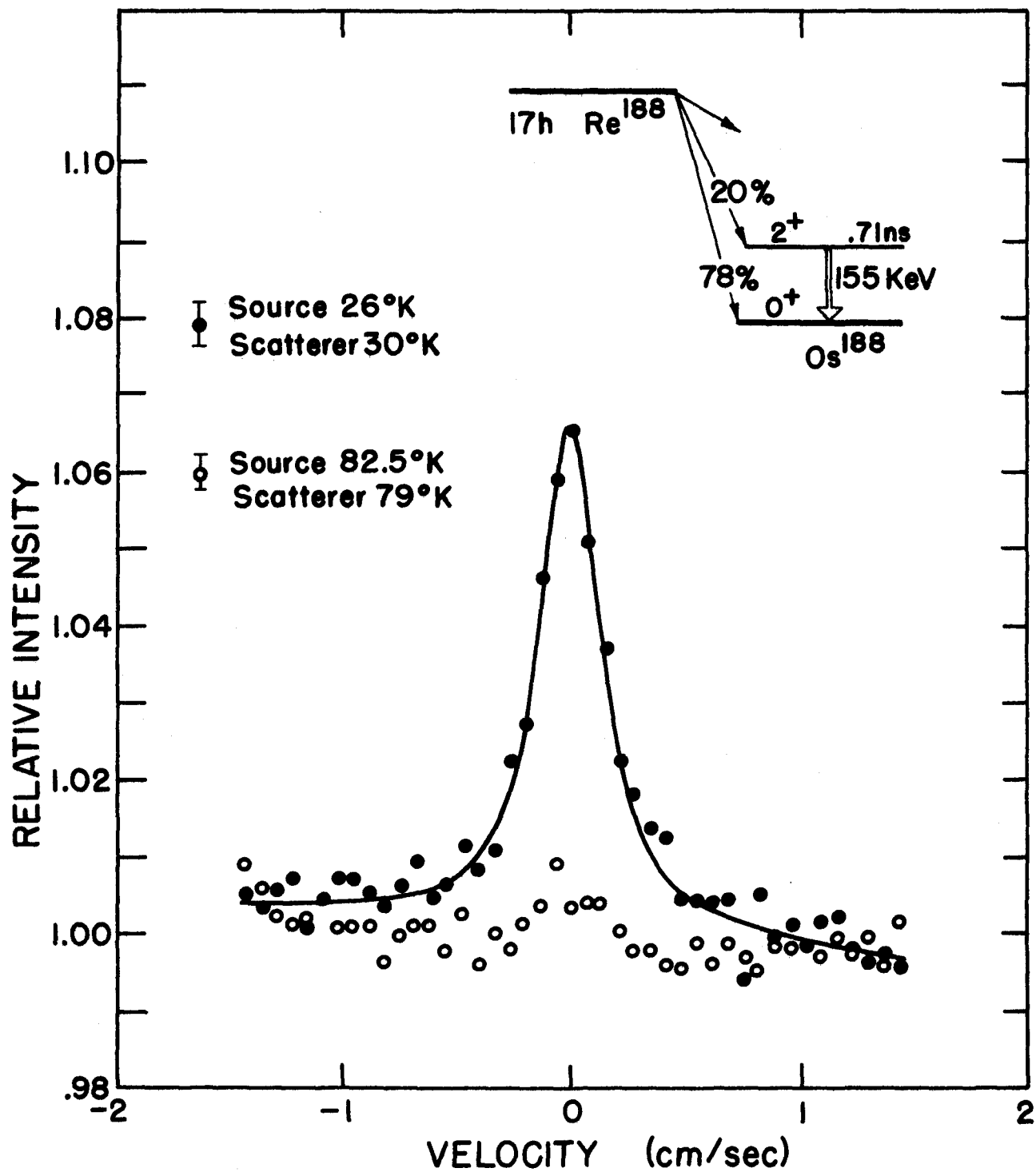
Fig. 14. The scattered count rate for the 155 keV transition of Os[188] as a function of the effective scatterer velocity.

Table 1

| Run | E , keV | Source Temp, $^{\circ}$K | Scatterer Temp, $^{\circ}$K | $\dfrac{f\overline{F(0,\lambda,A,\Gamma/\Gamma')}}{(1+\alpha)}$ |
|---|---|---|---|---|
| 1 | 137 | $26 \pm 5$ | $30 \pm 5$ | $(6.00 \pm 0.7)10^{-4}$ |
| | | $82.5 \pm 4.5$ | $79 \pm 1$ | $(1.35 \pm 0.16)10^{-4}$ |
| 2 | 155 | $26 \pm 5$ | $30 \pm 5$ | $(14.5 \pm 0.2)10^{-4}$ |
| | | $82.5 \pm 4.5$ | $79 \pm 4.5$ | $(1.5 \pm 0.4)10^{-4}$ |
| 3 | 137 | $8 \pm 4$ | $21 \pm 2$ | $(7.7 \pm 1.5)10^{-4}$ |
| | | $70 \pm 2$ | $21 \pm 2$ | $(3.9 \pm 0.8)10^{-4}$ |

Since the geometry was unchanged for the two runs, and for both sets of temperatures of each run, the ratios of the resonantly scattered intensities were independent of the geometrical factor. For the low temperature measurements the ratio of the reduced intensities for the two isotopes,

$$\frac{f^{155} \; F_{155}(0, \lambda, A, \Gamma/\Gamma')}{(1 + \alpha_{155})} \bigg/ \frac{f^{137} \; F_{137}(0, \lambda, A, \Gamma/\Gamma')}{(1 + \alpha_{137})} \; ,$$

had the value 2.43 ± 0.17. The ratio of the resonantly scattered intensities for a given isotope for two sets of temperatures was independent of the geometrical factor and the source intensity, and had a negligible dependence on $\alpha$. The value of this quantity,

$$\frac{f(82.5°) \; \overline{F(0, \lambda(79°), A, \Gamma/\Gamma')}}{f(26°) \; \overline{F(0, \lambda(30°), A, \Gamma/\Gamma')}} \; ,$$

for $Os^{186}$ was .23 ± 0.03.

In the analysis of the results the assumption was made that source and scatterer had the same Debye temperature. To check this assumption run 3 was made with $Os^{186}$ for two source temperatures $8°$ K and $70°$ K and a constant scatterer temperature of $21°$ K. The values for $f\overline{F(0, \lambda, A, \Gamma/\Gamma')}/(1+\alpha)$ are given in table 1. The ratio,

$$\frac{f^{137}(8°) \; \overline{F(0, \lambda(21°), A, \Gamma/\Gamma')}}{f^{137}(70°) \; \overline{F(0, \lambda(21°), A, \Gamma/\Gamma')}} = \frac{f^{137}(8°)}{f^{137}(70°)}$$

was 1.96 ± 0.08.

## 4.2 Discussion of the Results

4.21. Recoilless Fractions and Debye Temperatures. The sizable effects observed for the 137 and 155 keV transitions made possible a careful study of the recoilless fractions for these cases of high free nucleus recoil energy $E_R$ (Eq. (1-2)). The recoilless fractions were computed from the values of $\dfrac{f\, F(0,\lambda,A,\Gamma/\Gamma')}{(1+\alpha)}$ by the method of Sec. 2.4. Using

$$\beta_{NR}^2 = 1 + \frac{f'h}{Me}\, 2\pi \lambda^2 \frac{2I_{exc}+1}{2I_{gr}+1} \frac{\Gamma_{nat}}{\Gamma'} \frac{1}{1+\alpha} \frac{1}{\sqrt{(1+\sin\gamma_1 \cosec\gamma_2)}} \qquad (4\text{-}2)$$

and the curves of $F(0,\lambda,A,I)$ for the appropriate values of A we evaluated $\dfrac{f f'}{(1+\alpha)^2}$. By using the theoretical values $\alpha_{137} = 1.30$ and $\alpha_{155} = 0.82$[26,27] we then determined the product ff' for each $E_R$ and for each set of temperatures.

In order to separately determine the recoilless fractions of the source and scatterer another relationship was necessary. The Debye model is generally used to predict the dependence of the recoilless fraction on the properties of the lattice and on the temperature and free recoil energy. With this model the recoilless fraction is given[1]

$$f = e^{-\frac{3}{2}\frac{E_R}{k\theta_0}P\left(\frac{\theta_0}{T}\right)} \qquad (4\text{-}3)$$

where the Debye temperature $\theta_0$ contains the lattice properties, k is the Boltzman constant, and $P\left(\frac{\theta_0}{T}\right)$ is given by

$$P\left(\frac{\theta_0}{T}\right) = 1 + \frac{4T^2}{\theta_0^2}\int_0^{\theta_0/T} \frac{x}{e^x - 1}\, dx \; . \qquad (4\text{-}4)$$

We used this expression for the recoilless fractions and made the additional assumption that the Debye temperatures for the source and scatterer were the same. This assumption should be relatively good since rhenium and osmium metals have similar lattice properties.

Using this assumption we then solved for the value of $\theta_D$ which would give agreement with the scattered intensity for each set of data. These values of $\theta_D$ and the corresponding recoilless fractions are given in table 2.

The Debye model gives a simple prediction for the ratio of the recoilless fractions for two different recoil energies. The ratio,

$$\frac{f^{137}(26^0) f'^{137}(30^0)}{f^{155}(26^0) f'^{155}(30^0)} )$$

was determined from the ratio of the scattered intensities for the two energies. In terms of the Debye model we have the relationship

$$Log\left[\frac{f^{137}(26^0) f'^{137}(30^0)}{f^{155}(26^0) f'^{155}(30^0)}\right] = -\frac{3/2\left[E_R^{137} - E_R^{155}\right]}{k\,\theta_D}\left[P\left(\frac{\theta_D}{26}\right) + P\left(\frac{\theta_D}{30}\right)\right]. \quad (4\text{-}5)$$

The value of $\theta_D$ which was in agreement with these results was $\theta_D = (374 \pm 18)^0$ K.

A comparison of the temperature dependence of f with the prediction of the Debye model was made by using the ratio of the scattered intensities for the same $E_R$ but for different temperatures. This was done for the $Os^{186}$ case for the set of results where both source and scatterer temperatures were varied. From the ratio of scattered intensities we determined $\theta_D = (358 \pm 16)^0$ K. The most accurate measurement made with the osmium isotopes was the ratio of the scattered intensities for the second set of measurements with $Os^{186}$. Since the scatterer temperature was constant this ratio gave directly the ratio of the recoilless fractions for the source for $T = 8^0$ K and $T = 70^0$ K. This ratio is in agreement with the predictions of the Debye model if $\theta_D = (350 \pm 16)^0$ K. This agreement with the result $\theta_D = (358 \pm 16)^0$ K supports the assumption of equal Debye temperatures for source and scatterer.

From these results we conclude that the Debye theory gives only qualitatively correct predictions for the recoilless fractions. The effective Debye temperature increases with both temperature and recoil energy.

Table 2

Recoilless fractions f and Debye temperatures $\theta_D$ for the two gamma ray energies $E_\gamma$ as determined from the scattered intensities assuming that $\theta_D$ is the same for source and scatterer for each set of temperatures.

| E , keV | $\theta_D$, deg K | T, deg K | f |
|---------|-------------------|----------|---|
| 137 | 312 ± 7 | 26 ± 5 | .043 ± .003 |
| | | 30 ± 5 | .041 ± .003 |
| | 330 ± 9 | 79 ± 1 | .021 ± .002 |
| | | 82.5 ± 4.5 | .019 ± .002 |
| 155 | 322 ± 7 | 26 ± 5 | .021 ± .002 |
| | | 30 ± 5 | .020 ± .002 |
| | 328 ± 11 | 79 ± 1 | .0071 ± .001 |
| | | 82.5 ± 4.5 | .0063 ± .001 |
| 137 | 314 ± 14 | 8 ± 4 | .049 ± .003 |
| | | 21 ± 2 | .046 ± .003 |
| | 320 ± 14 | 70 ± 2 | .022 ± .004 |
| | | 21 ± 2 | .049 ± .003 |

4.22 <u>Shifts</u> <u>and</u> <u>Broadenings</u>. The absence of isomer shifts[*] with these isotopes is consistent with the predictions of the collective model of the nucleus. The isomer shift is given to a good approximation[*] by

$$\delta = C \left[ |\psi'(0)|^2 - |\psi(0)|^2 \right] \frac{\delta R}{R} , \qquad (4\text{-}6)$$

where $\delta$ is the shift of the observed resonance in cm/sec, $|\psi'(0)|^2$ and $|\psi(0)|^2$ are the electron densities at the nucleus for scatterer and source, respectively, $\frac{\delta R}{R}$ is the fractional difference between the charge radii of the excited and ground state nuclei respectively.[**] The constant C is given in the nonrelativistic approximation

$$C = \frac{4\pi Z e^2 R^2}{5} \frac{c}{E_\gamma} ,$$

where Z is the atomic number and e is the electron charge. Velocities are defined to be positive for relative motion of the scatterer toward the source. The 137 and 155 keV states are identified in the collective model as rotational excitations of the ground intrinsic states. To the extent that the collective model is valid, the charge radii and the deformations should be the same for the excited and ground states and no isomer shift should be observed.

If we assume that the observed broadening is due to an unresolved electric quadrupole splitting,

$$\Delta E_J = \frac{e^2 q Q}{4} \left[ \frac{3 m_j^2 - I(I+1)}{I(2I-1)} \right] , \qquad (4\text{-}7)$$

we can calculate a value for the electric field gradient in osmium. In this expression, which is valid for axially symmetric field gradients,

---

[*]For a complete description of the isomer shift see Shirley.[28]

[**]For deformed nuclei the isomer shift can result from a change in deformation as well as from a change in charge radius. This is discussed by Shirley.[28]

$\Delta E_j$ is the energy shift of the $j^{th}$ hyperfine level, Q is the quadrupole moment for the nuclear state, eq is the field gradient at the nucleus, and $m_j$ is the z component of the nuclear spin I. The field gradients in osmium and rhenium are axially symmetric as a result of the hexagonal crystal structure. From the known value of the intrinsic quadrupole moment, $Q_0 = 6.2 \ 10^{-24} \ cm^2$ [29], the value of Q for the $2^+$ level was calculated with the expression [30],

$$Q = Q_0 \frac{3K^2 - I(I+1)}{(I+1)(2I+3)} ) \tag{4-8}$$

which is valid for members of a rotational band. Here K is the projection of I on the nuclear symmetry axis and is zero for this case. Using the value of rhenium $eq_{re} = 4.05 \ 10^{17} \ V/cm^2$ [31] and our value for the broadening of the line we found $eq_{os} = (6.5 \pm 1.0) \ 10^{17} \ V/cm^2$. This result is equal to the field gradient that one obtains from the value for rhenium by simply changing the lattice contribution according to the larger c/a ratio for osmium. [31]

## 5. MÖSSBAUER SCATTERING WITH Eu[153] AND Pr[141]

The properties of the Eu[153] and Pr[141] level schemes (Figs. 15 and 16) make these isotopes attractive for Mössbauer scattering experiments. About 78% of the beta decays of the Sm[153] parent result in a 103 keV Eu[153] gamma ray. The Ce[141] source has a 70% branching to the 145 keV level of Pr[141] with the remainder of the decays going directly to the ground state. Both the Sm[153] and Ce[141] sources are characterized by small amounts of internal Bremsstrahlung and have low intensities of gamma rays of energies higher than the 103 and 145 keV transitions used in the experiments. The natural widths of these lines, as determined from the halflives of 3.5[32, 33)] and 2.0[34)] nsec, are sufficiently narrow to permit the study of isomer shifts and hyperfine splittings.

### 5.1 Experimental Results

5.11 Sm$_2$O$_3$ and SmF$_3$ Sources with an Eu$_2$O$_3$ Scatterer. A 31% single line resonant peak was observed with an Sm$_2$O$_3$ source at $(30 \pm 10)^\circ$ K and an Eu$_2$O$_3$ scatterer at $(30 \pm 5)^\circ$ K. The scatterer consisted of a 0.3 g/cm$^2$ layer of Eu$_2$O$_3$ cemented to the entire inner surface of the scatterer support. The resonant peak was observed to have a width of $(0.21 \pm 0.01)$ cm/sec and was shifted by $(-0.045 \pm 0.005)$ cm/sec. The velocity is defined to be positive when the scatterer moves toward the source. The scattered intensity was also measured for scatterer and source temperatures of 80° K.

Measurements were also made with an SmF$_3$ source at $(23 \pm 2)^\circ$ K and an Eu$_2$O$_3$ ring scatterer (Sec. 3.2) at $(22 \pm 2)^\circ$ K. The 18.6% single peak
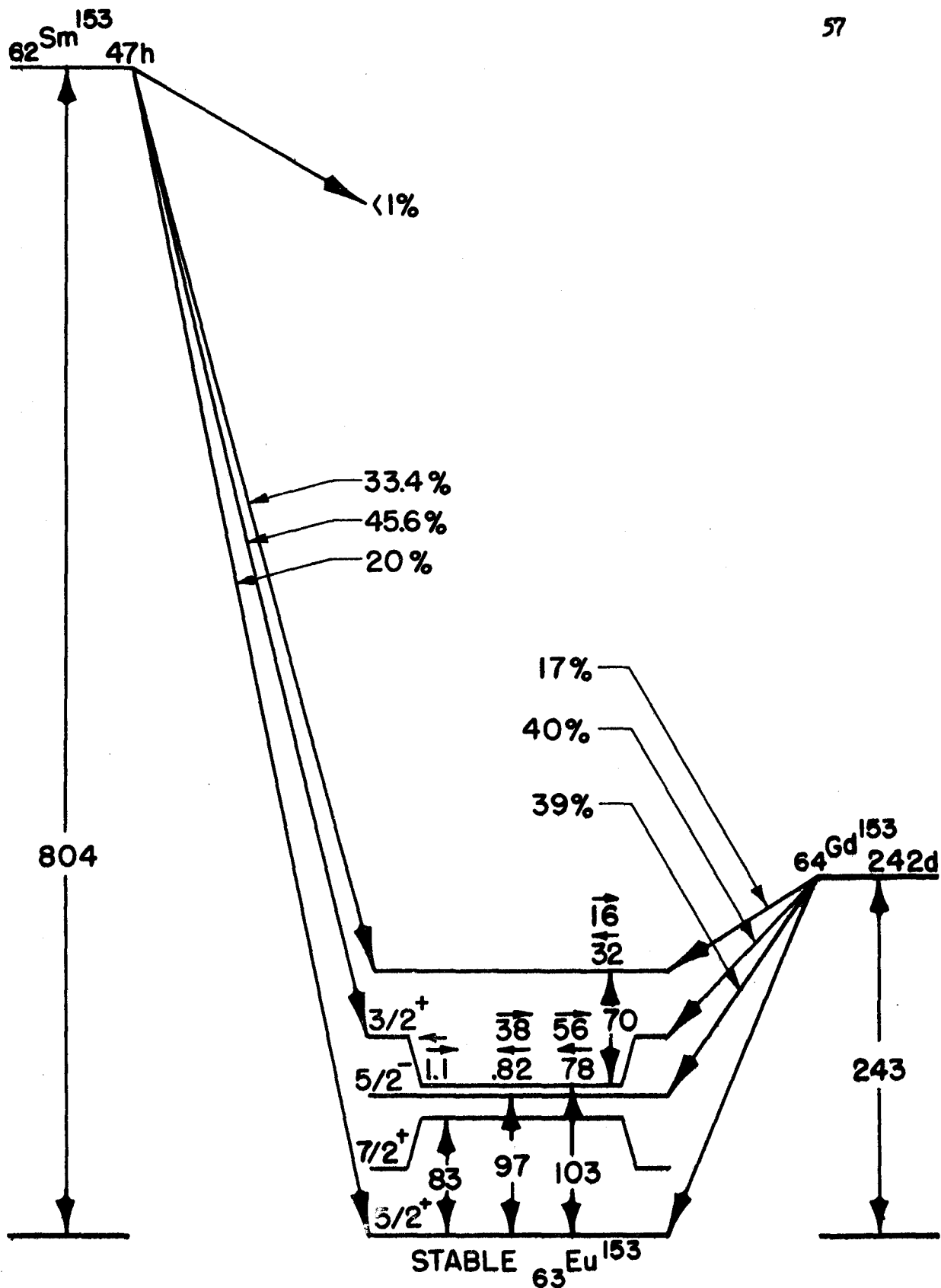
Fig. 15. The Eu[153] decay scheme. Energies are in keV. The numbers under the small arrows indicate the number of transitions per 100 decays of the respective parent isotope.
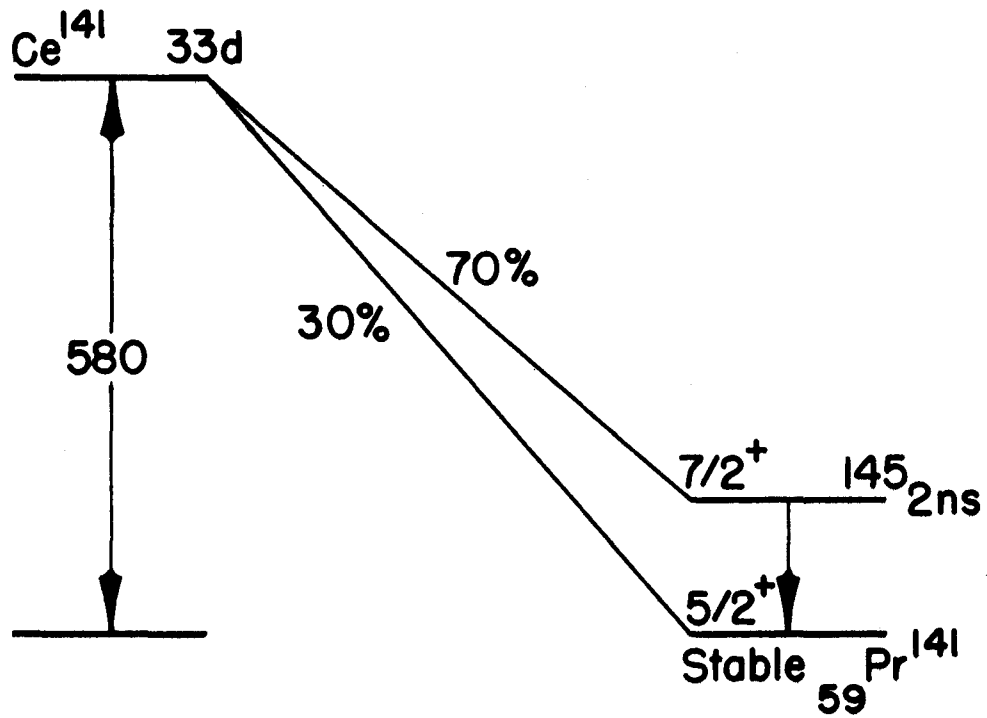
Fig. 16. The Pr$^{141}$ decay scheme. Energies are in keV.

observed had a larger width $(0.27 \pm 0.03)$ cm/sec and a larger shift $(-0.12 \pm 0.02)$ cm/sec than was observed with the $Sm_2O_3$ source.

5.12 $\underline{Sm_2O_3}$ $\underline{Source}$ $\underline{with}$ $\underline{an}$ $\underline{Europium}$ $\underline{Iron}$ $\underline{Garnet}$ $\underline{Scatterer}$. In order to obtain a value for the magnetic moment of the 103 keV level of $Eu^{153}$, measurements were made with a ferrimagnetic scatterer. To obtain a resolved magnetic hyperfine splitting with typical experimental line widths of 0.21 cm/sec $(0.73 \ 10^{-6} ev)$ it was necessary to have a scatterer with an effective magnetic field at the nucleus $H_{eff} \sim 10^6$ Oe. Magnetic fields at the center of rare earth ions are frequently larger than this because the orbital angular momentum of the unfilled 4f shell is unquenched.[35] Few europium compounds or alloys exhibit a large $H_{eff}$, however, because the ground state of the common $3^+$ ion is $^7F_0$.[36] The hyperfine field is proportional to the z component of the total angular momentum which is zero for this case. In europium iron garnet (EuIG), however, the strong exchange interaction of the iron sublattice causes a sufficient admixture of the excited $^7F_1$ atomic state into the $^7F_0$ state to produce a sizable field.[37] This field has been studied with the Mössbauer effect in the $Eu^{151}$ isotope and has been found to be $(585 \pm 15) \ 10^3$ Oe.[38, 39]

Measurements were made with a 0.5 $g/cm^2$ ring scatterer of EuIG at $(17 \pm 2)^\circ$ K. The $Sm_2O_3$ source had a temperature $(15 \pm 2)^\circ$ K. The results for one polarity of the pickup signal are shown in Fig. 17. Approximately the same number of counts were taken with the polarity reversed. Data was taken with larger velocities but no other lines were observed.

Fig. 17. The magnetic hyperfine spectrum for a single line
$Sm_2O_3$ source and a ferrimagnetic europium iron garnet
scatterer. The curve of the scattered count rate vs.
the effective scatterer velocity is shown. The effec-
tive scatterer velocity is the rod velocity divided by
1.25 and is positive for the scatterer moving toward
the source. The data have been slope-corrected and
the background is normalized to 1. The solid line is
the result of the least square fit.
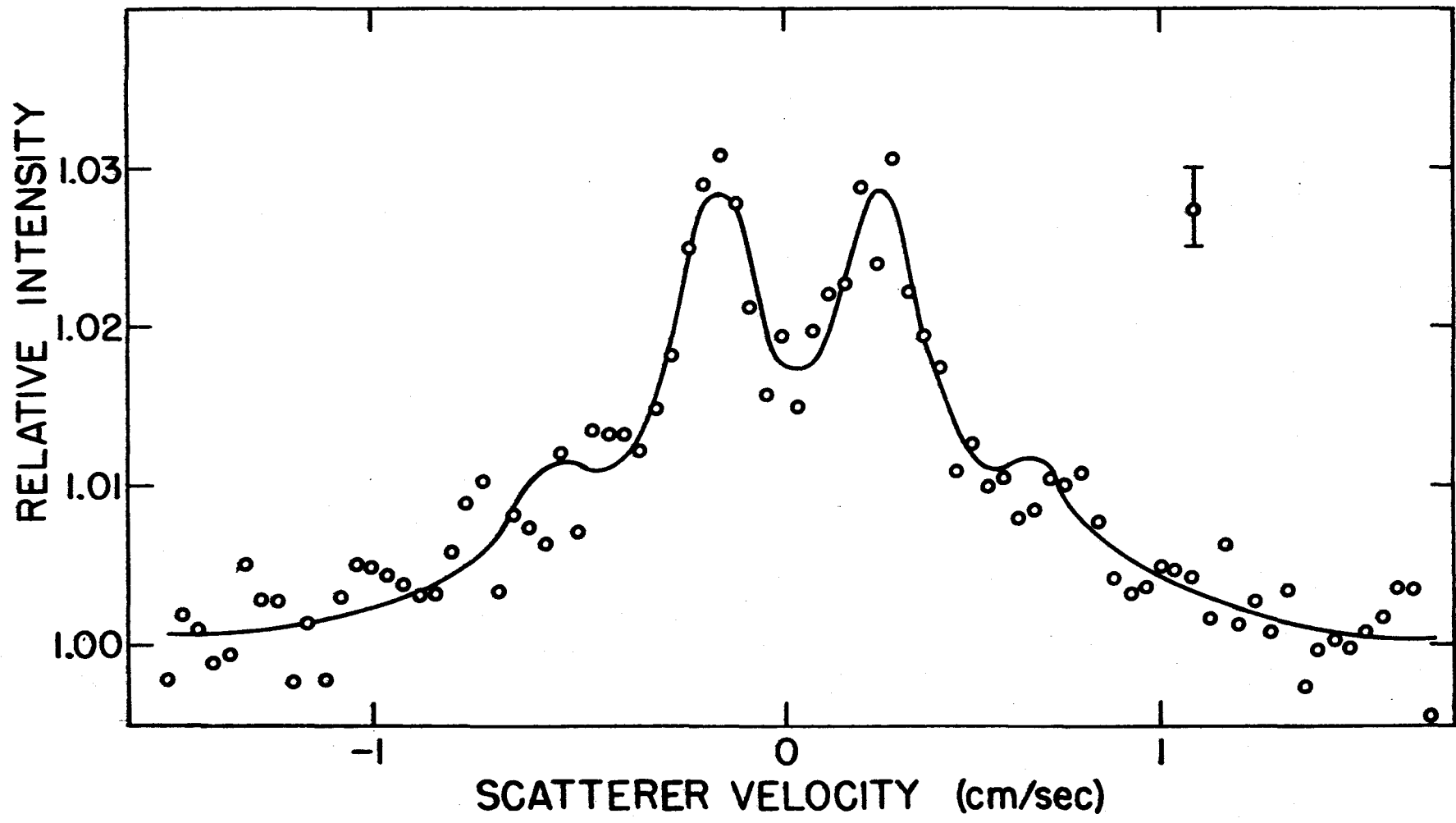
5.13 $Pr^{141}$ Results. Single resonant peaks of about 4% and 3% of the background level were observed with $CeO_2$ and $CeF_3$ sources at $(15 \pm 3)^\circ$ K and a .45 $g/cm^2$ scatterer of $Pr_6O_{11}$ at $(17 \pm 2)^\circ$ K. The lines observed had widths that were larger by factors of 3.0 and 2.0 respectively than the natural widths calculated from the 2.0 nsec half-life of the state.

## 5.2 Discussion of the Results

### 5.21 Recoilless Fractions and Debye Temperatures.

The recoilless fractions were evaluated from the scattered intensities by the method of Sec. 2.4. In order to evaluate the recoilless fractions of $Sm_2O_3$ and $Eu_2O_3$ we assumed that for a given temperature both materials have the same Debye temperature and that the resonance lines are broadened by the same factor of 2.75. Using the value $1.50 \pm 0.15$[40] for the conversion coefficient we found the recoilless fraction at $30^\circ$ K to be $(3.5 \pm 0.7)$ $10^{-2}$ with a corresponding Debye temperature, $\theta_D = (215 \pm 15)^\circ$ K. This result is in good agreement with the value $\theta_D = 225^\circ$ K found by Atzmomy, Mualem and Ofer.[41] Using $\theta_D = 215^\circ$ K for the $Sm_2O_3$ source and $Eu_2O_3$ scatterer we then found larger values $\theta_D = (340 \pm 80)^\circ$ K and $\theta_D = (270 \pm 40)^\circ$ K for the EuIG scatterer and the $SmF_3$ source respectively.

We also evaluated the Debye temperature from the ratio of the scattered intensities for the $Sm_2O_3$ source and the $Eu_2O_3$ scatterer for the two sets of temperatures. The value $\theta_D = (263 \pm 20)^\circ$ K was in agreement with the observed temperature dependence.

The recoilless fractions calculated from the Praseodymium results are surprisingly large. Using the value $\alpha = 0.46$[42, 43] we found that the product of the recoilless fractions for the $CeO_2$ source and the $Pr_6O_{11}$ scatterer was $(2.4 \pm 1.2)$ $10^{-5}$. We then have average values $\bar{f} = 0.0049 \pm 0.0012$ and $\bar{\theta}_D = (270 \pm 20)^\circ$ K for the two lattices. The

recoilless fractions and the Debye temperatures were nearly the same for the results with the $CeF_3$ source.

The values for Debye temperatures and recoilless fractions found with the $Eu^{153}$ and $Pr^{141}$ isotopes were higher than we had expected. The expectations were based on earlier experiments by Shirley and coworkers[44] with the 21.7 keV transition in $Eu^{151}$. From their transmission experiments with sources and absorbers of $Eu_2O_3$ they found a Debye temperature for $Eu_2O_3$ which increased from $65^{\circ}$ at $4^{\circ}$ K to $185^{\circ}$ at $300^{\circ}$ K. Using their value for $\Theta_D$ at $4^{\circ}$ K one would expect the recoilless fractions for the 103 keV transition with the lattices $Eu_2O_3$ and $Sm_2O_3$ to be less than $10^{-5}$. A higher Debye temperature has been reported for the similar $Gd_2O_3$ lattice. Ofer and coworkers[45] have studied the Mössbauer effect with the 26 keV transition in $Dy^{161}$. Their results with a $Tb^{161}$ source in a $Gd_2O_3$ lattice at room temperature indicate a Debye temperature $\Theta_D = 230^{\circ}$ K. Shirley's high temperature value $\Theta_D = 185^{\circ}$ K and the Debye temperatures found with $Dy^{161}$ and $Eu^{153}$ appear to be roughly consistent. There is striking disagreement, however, between the low temperature values, $\Theta_D = 65^{\circ}$ K and $\Theta_D \sim 220^{\circ}$ K found with the $Eu^{151}$ and $Eu^{153}$ isotopes respectively.

On the basis of the work done with $Eu^{153}$ the result of $\Theta_D = 65^{\circ}$ K at $4^{\circ}$ K seems questionable. If we accept this value however we are faced with an interesting question about the inter-atomic forces in the lattice. The recoilless fraction can be expressed in the form

$$f = e^{-E_R G(T, \rho(\omega))}, \qquad (5\text{-}1)$$

where $G(T, \rho(\omega))$ is a function of the temperature and the density of phonon states, but does not depend upon the energy of the emitted gamma ray. The only assumption that has been used in the derivation of

Eq. (5-1) is that the lattice forces are harmonic.[46,47] To

the extent that Eq. (5-1) is valid the effective Debye temperatures ob-

served should be independent of the energy of the gamma ray transition.

The larger effective Debye temperatures observed for the higher transi-

tion energies would indicate that the recoilless fractions show a strong

dependence on anharmonic lattice forces.

### 5.22 The Magnetic Moment of the 103 keV Eu[153] State.

The complete

interpretation of the results with the EuIG scatterer must include the

possibilities of a quadrupole interaction and an isomer shift in addition

to the magnetic hyperfine interaction. The energy shift of the $j^{th}$ line

is than given by

$$\delta E_j = \delta E - \mu_0 H_{eff}(g m_j - g^* m_j^*) +$$
$$\frac{1}{4} e^2 q \left[ Q \frac{3 m_j - I(I+1)}{I(2I-1)} - Q^* \frac{3 m_j^* - I^*(I^*+1)}{I^*(2I^*-1)} \right]_j \quad (5-2)$$

where $\delta E$ is the isomer shift, $\mu_0$ is the nuclear magneton, g and g* are

the g factors of the ground and excited states, eq is the electric field

gradient at the nucleus, Q and Q* are the quadrupole moments of the

ground and excited states, I and I* are the spins of the states with z

components $m_j$ and $m_j^*$. Twelve lines are expected for the predominantly

M1 transitions between the 5/2 and 3/2 ground and excited states. In

Fig. 18 the relative positions of the lines, under the assumption that

quadrupole interactions can be neglected, are shown as a function of g*/g.

The data were least square fitted to a superposition of twelve

Lorentzian lines with relative positions given by Eq. (5-2) and with

the relative intensities given by the square of the appropriate Clebsch-

Gordan coefficients. The result of one of the fits is shown in Fig. 17.

From the fits we found that the quadrupole couplings $e^2qQ$ and $e^2qQ^*$ were

Fig. 18.   The g-factor diagram for the case of ground and excited
state spins 5/2 and 3/2 respectively.  The positions,
$(m_j - \frac{g^*}{g} m_j^*)$, of the 12 lines to be expected for M1
transitions are shown as a function of $g^*/g$.  Electric
quadrupole effects have not been included.
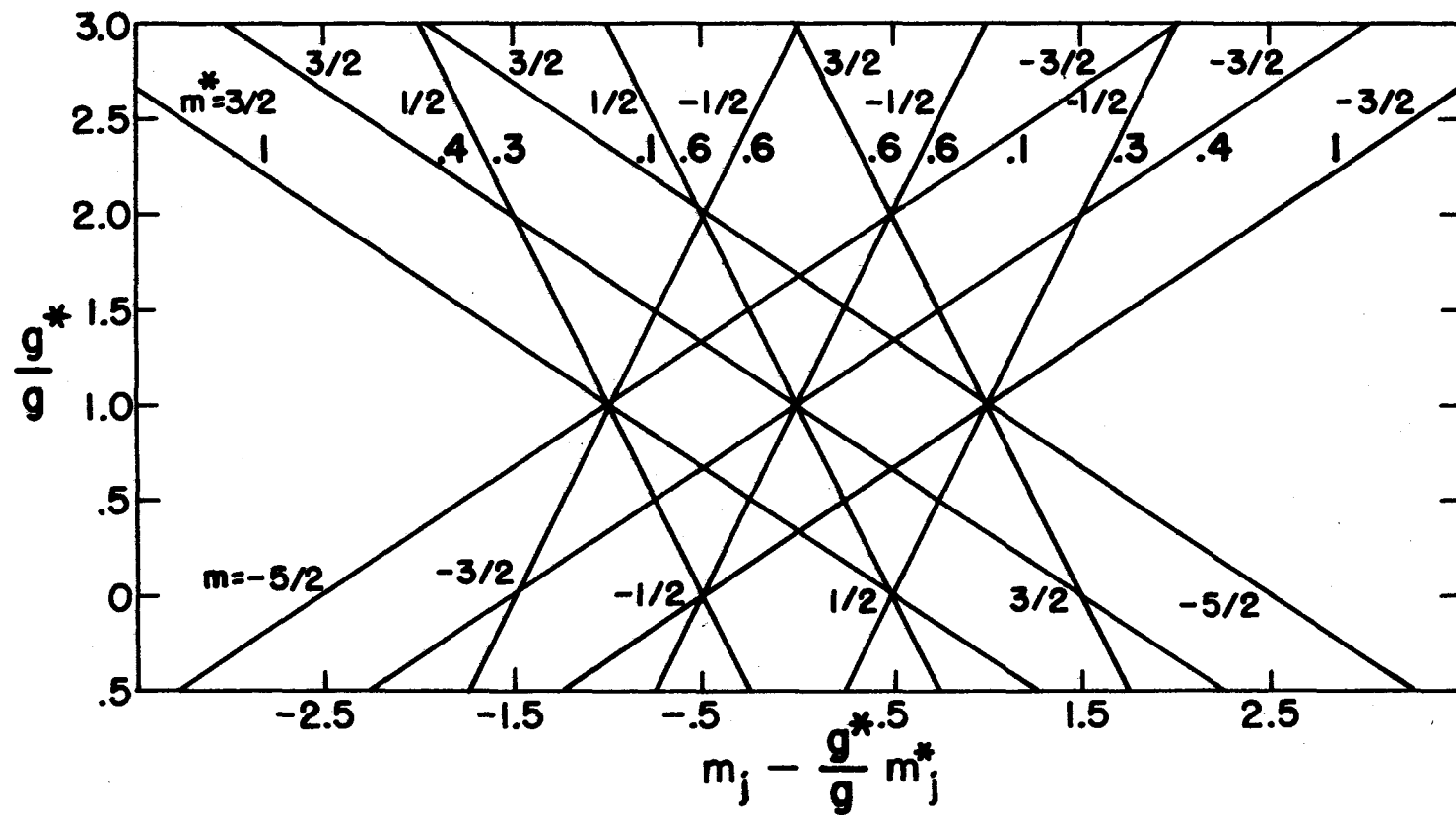
less than $10^{-7}$ eV. The shift of the center of the spectrum was observed to be $(0.036 \pm 0.006)$ cm/sec. The values obtained for $g^*/g$ were 2.05. and 2.14 for the two sets of data. By averaging the values we obtained $g^*/g = 2.1 \pm 0.2$.

Using the value for the magnetic moment of the ground state $\mathcal{M} = (1.507 \pm 0.003)$[48] n m we then found the value for the excited state magnetic moment $\mathcal{M}^* = (1.90 \pm 0.2)$ n m. This value was obtained without making any assumptions about the magnitude of the magnetic field at the nucleus. Atzmony, Mualem, and Ofer[41] applied the additional constraint $H_{eff} = 585$ kOe to their fit and obtained the value $\mathcal{M}^* = (2.01 \pm 0.09)$ n m.

# BIBLIOGRAPHY

1. Hans Frauenfelder, The Mössbauer Effect (W.A. Benjamin, Inc., New York, 1962.

2. A. Boyle and H. Hall, Rept. Prog. Phys. 25, 441 (1962).

3. R.L. Mössbauer and W.H. Wiedemann, Z. Physik 159, 33 (1960).

4. P.H. Barrett and L. Grodzins, Revs. Modern Phys. 36, 471 (1964).

5. P.H. Barrett, Perturbed Angular Correlations (North Holland Publishing Co., Amsterdam, 1964), p. 306.

6. P. Debrunner and R.J. Morrison, to be published.

7. A. Bussiere De Nercy, M. Langevin, and M. Spighel, J. Phys. Rad. 21, 288 (1960).

8. A. Bussiere De Nercy, M. Langevin, and M. Spighel, Compt. Rend. 250, 1031 (1960).

9. R.J. Morrison, M. Atac, P. Debruner and H. Frauenfelder, Phys. Letters 12, (1964) Sept.

10. J.K. Major, Nuclear Physics 33, 323 (1962).

11. P. Debrunner and R.J. Morrison, Revs. Modern Phys. 36, 463 (1964).

12. P.J. Black, G. Longworth and D.A. O'Connor, Proc. Phys. Soc. 83, 937 (1964).

13. G.T. Trammel, Phys. Rev. 126, 1045 (1962).

14. C.T. Zara, J. Phys. Radium 22, 303, (1961).

15. H.J. Lipkin, Phys. Rev. 123, 62 (1961).

16. J.D. Jackson, Can. J. Phys. 33, 575 (1955).

17. W.E. Lamb, Jr., Phys. Rev. 55, 190 (1939).

18. D.A. O'Connor and P.J. Black, Proc. Phys. Soc. 83, 941 (1964).

19. W. Franz, Z. Physik 98, 314 (1935).

20. P.B. Moon, Proc. Phys. Soc. (London) 63A, 1189 (1950).

21. S. Margulies and J.R. Ehrman, Nucl. Inst. and Meth. 12, 131 (1961).

22. S. Margulies, P. Debrunner and H. Frauenfelder, Nucl. Inst. and Meth. 21, 217 (1963).

23. E. Kankeleit, Revs. Sci. Intr. 35, 194 (1964).

24. E. Bodenstedt, H.J. Körner, G. Strube, C. Günther, J. Radeloff and E. Gerdau, Z. Physik 163, 1 (1961).

25. D.B. Fossan and B. Herskin, Nuclear Phys. 40, 24 (1963).

26. M.E. Rose, Internal Conversion Coefficients (North Holland Publishing Company, Amsterdam, 1958).

27. L.A. Sliv and J.M. Band, Internal Conversion Coefficient Tables, circulated by the University of Illinois.

28. D.A. Shirley, Rev. Modern Phys. 36, 333 (1964).

29. D.H. Rester, M.S. Moore, F.E. Durham and C.M. Class, Nuclear Phys. 22, 104 (1961).

30. A. Bohr and B.R. Mottelson, Kgl. Danske Videnskab. Selskab Mat. fys. Medd. 27, No. 16 (1953).

31. T.P. Das and M. Pomerantz, Phys. Rev. 123, 2070 (1961).

32. P. Reyes-Suter and T. Suter, Arkiv Fysik 20, 399 (1961).

33. T.D. Nainan, Phys. Rev. 123, 1751 (1961).

34. H. deWaard and T.R. Gerholm, Physica 21, 599 (1955).

35. J. Kondo, J. Phys. Soc. Japan 16, 1690 (1961).

36. Karl A. Gschneidner, Jr., Rare Earth Alloys (D. Van Nostrand, Inc., Princeton, 1961), p. 42.

37. W.P. Wolf and J.H. Van Vleck, Phys. Rev. 118, 1490 (1960).

38. P. Kienle, Rev. Modern Phys. 36, 372 (1964).

39. I. Nowik and S. Ofer, Phys. Rev. 132, 241 (1961).

40. T. Suter, P. Reyes-Suter, S. Gustafsson, I. Marklund, Nuclear Phys. 29, 33 (1962).

41. U. Atzmony, A. Mualem and S. Ofer, Personal Communication.

42. L. Nement, Izvest, Akad. Nauk SSSR, Sera Fiz. 25, 68 (1961).

43. J.R. Cook, Proc. Phys. Soc. (London) 77, 346 (1961).

44. D.A. Shirley, R.B. Frankel, and H.H. Wickman, Rev. Modern Phys. 36, 392 (1964).

45. S. Ofer, P. Avivi, R. Bauminger, A. Marinov and S.G. Cohen, Phys. Rev. 120, 406 (1960).

46. Harry J. Lipkin, Ann. Phys. 9, 332 (1960).

47. Yu. Kagan, JETP 13, 211 (1961).

48. M. Pichanick, P.G.H. Sanders and G.U. Woodgate, Proc. Soc. (London) 257, 277 (1960).

VITA

He
received a Bachelor of Arts degree in physics and mathematics from the
Ohio Wesleyan University in June, 1959.  He began graduate study in
physics at the University of Illinois in September 1959 where he held the
position of teaching assistant until June, 1961.  During the summer of
1960, and continuously since June, 1961, he has been a research assistant
working with Professors Hans Frauenfelder and Peter Debrunner on Mössbauer
Scattering.  He received the Master of Science degree in physics from the
University of Illinois in February, 1961.